Supplemental information

Pyrolytic fragmentation-induced defect formation in formamidinium lead halide perovskite thin film and photovoltaic performance limits

Byung-wook Park[1 #*], Geonhwa Kim[2#], Chinnathambi Kamal[3,4#], BongJin Simon Mun[5], Ute B. Cappel[6], Håkan Rensmo[6], Ki-Jeong Kim[2*], Michael Odelius[7*], Sang Il Seok[1*]

[1]Department of Energy and Chemical Engineering, Ulsan National Institute of Science and Technology (UNIST), 50 UNIST-gil, Eonyang-eup, Ulju-gun, Ulsan 44919, Republic of Korea

[2]Beamline Research Division, Pohang Accelerator Laboratory (PAL), Pohang University of Science and Technology (POSTECH), Pohang 37673, Republic of Korea

[3]Theory and Simulations Laboratory, Theoretical and Computational Physics Section, Raja Ramanna Centre for Advanced Technology, Indore - 452013, India

[4]Homi Bhabha National Institute, Training School Complex, Anushakti Nagar, Mumbai-400094, India

[5]Department of Physics and Photon Science, Gwangju Institute of Science and Technology (GIST), Gwangju 61005, Republic of Korea

[6]Condensed Matter Physics of Energy Materials, Division of X-ray Photon Science, Department of Physics and Astronomy, Uppsala University, Box 516, 75120 Uppsala, Sweden

[7]Department of Physics, AlbaNova University Center, Stockholm University, 106 91 Stockholm, Sweden

Co-first author [#] : Byung-wook Park, Geonhwa Kim, Chinnathambi Kamal

Corresponding authors * : sapgreen79@unist.ac.kr, kjkim@postech.ac.kr, odelius@fysik.su.se , seoksi@unist.ac.kr

Content S1. Microstrain (ε_{wh}) and dislocations (ρ_d)

The ε_{wh} as mean square strain is referred to degree of line defects as ρ_d in the crystal[Refs. S1, 2]. The crystal of size below 20 nm is mostly not considered due to very difficult to observe dislocations by transmission electron microscopy[Ref. S3]. In this basis, for five cyclic steps of post-annealing such as 25 °C (step 0, denoted by $S0_m$), 150 °C ($S1_m$), 200 °C ($S2_m$), 250 °C ($S3_m$), and 300 °C ($S4_m$) as displayed in Fig. S3, we derived crystallite size (Fig. S6(a)), ε_{wh} (Fig. S6(b)) based on the Williamson-Hall plots (Figs. S7 and S8) and calculated ρ_d (Figs. S6(c,d)) at two depths of the model metal halide perovskite (MHP_m) film. To calculate crystallite sizes at two film depths, surface condition as the depth of 10 nm is smaller length than its crystallite size that is allowed to observe clearer effects for generation/annihilation of small quantity of local δ-$FAPbI_3$ phase as intraplanar defect (denoted as IPD) with changing trends of ε_{wh} and ρ_d in the crystallites, comparing to those values at full depth condition. The values of ε_{wh} exhibited an overall trend towards compressive condition due to the relatively high ρ_d. The sum of ε_{wh} at two depth conditions (an averaged ε_{wh}) rapidly weakens from the $S1_m$, indicating a reduction in ρ_d, as a general tendency. Upon closer examination of the comparison between the surface and full-depth, the defined ε_{wh} for full-depth was found to be around 180% (an average value of all post-annealing conditions) greater than that of the surface. Furthermore, we observed an interesting phenomenon: ρ_d decreased at full-depth while it increased at the surface. This result suggests that there is migration of the dislocation from near the electron transfer layer to the surface in the MHP_m film. Dislocations in perovskite crystal were also observed to migrate and change ρ_d under radiation condition[Ref. S3] and even under compressive strain/stress conditions of the crystal[Ref. S4]. In the context of the relationship between d-spacings and ε_{wh}, a strengthened ε_{wh} can lead to a reduction in d-spacings of α-$FAPbI_3$ indices. Moreover, we noted that weakened ε_{wh} increased ρ_d at both depths. In comparison between surface and full-depth in $\alpha(100)_c$, as shown in Fig. S6(c), when ρ_d increased at the surface and reduced ρ_d at full-depth in the same time as indicating the inversely proportional relation with two exceptional points at the $S1_m$ and $S2_m$. On the other hand, for ρ_d in $\alpha(200)_c$ at the same film depth conditions as shown in Fig. S6(d), we found a similar tendency as the indicated ρ_d changes with two exceptional points of $S2_m$ to the $S3_m$. Particularly at the surface in $\alpha(200)_c$, ρ_d was reduced by ~19.35% from the $S2_m$ to the $S3_m$, highlighting the primary dependency of ε_{wh} on the ρ_d. This miss-match tendency between ε_{wh} and ρ_d may be influenced by other factors related to defective crystals such as IPDs in the MHP_m film.

Content S2. Description of density functional theory (DFT)

We conducted DFT calculations of electronic density of state (DOS) in relation to N 1s core-level (Fig. S13 and Figs. 2(e,f)). Valence band spectra (Figs. S15-S17 and Fig. 3(a)) for five model systems where the pure $FAPbI_3$ model had 24 FA^+ molecules (with 48 nitrogen atoms) and the defect models contained such as 46 nitrogen atoms of 23 FA^+ molecules and one nitrogen atom of substituted (NH_3, NH_4^+, HCN, and $HCNH^+$) molecules in Fig. 2(d). The percentage of substituted by-products at the A-site in $FAPbI_3$ is about 4.17% (namely 1:24). The calculated discrete spectra were convoluted with a Gaussian function with 0.1 eV full-width of half-maximum. When NH_4^+ or $HCNH^+$ replaces a FA^+, the model supercell retains the neutral overall charge, and the long-range electrostatics is relatively unaffected. Therefore, the crystal structure only responded to the changes in local hydrogen bonding interactions and in the change in the molecular dipole of this A site. On the other hand, in cases of NH_3 and HCN substitutions, their charge states deviated from that of FA^+. Consequently, these two systems have a net negative total charge and expected to exhibit reduced ionic interactions, locally around the defect. The FA^+ and PbI_3^- frameworks conceptually represent single positively and negatively charged species, respectively. Consequently, FA^+ and PbI_3^- frameworks were used as the stabilized reference for the $FAPbI_3$ model system, ensuring a perfect charge balance and full occupancy of FA^+ at A site in PbI_3 framework. We generated five simulated N 1s and valence band spectra using these reference systems. The spectra obtained for the four defect model systems (Figs. S13 and S15-S17) are aligned at the peak of FA^+ (397.84 eV) for pristine $FAPbI_3$ as displayed in Figs. 2(e,f), and Fig. 3(a). In this simulation, we did not consider the effect of doped Br^- in the MHP_m film due to its very low concentration. Instead, our focus was solely on understanding the effects of substituted by-products at A site in the reference system. Before alignment, the simulated N 1s spectra for these model systems reveal a relatively small difference in the average binding energies (BEs) of N 1s of FA^+ molecules in pristine $FAPbI_3$ and four by-products substituted $FAPbI_3$. The core-level calculations of the defect models show some variation (within 0.2 eV in the BE of the FA^+ nitrogen atoms). This variation is due to an overall offset in the DOS due to the replicated defect in the periodic boundary conditions. This variation is due to an overall offset in the DOS due to the replicated defect in the periodic boundary conditions. Hence, we align the FA^+ peak and focus on the nitrogen atoms at larger BE shifts in the by-products.

Content S3. PES analysis for valence band (VB)

Before interpreting the experimental VB spectra, we acknowledge two important factors. Firstly, when interpreting these spectra, it is crucial to consider the high surface sensitivity for the VB spectra measured here. The probe depth is below 1 nm and consequently, any surface contamination, such as carbon-containing molecules common in these investigations or enrichment of the A site cation at the surface[Ref. S5]. Secondly, when making comparisons with theoretical calculations, it is crucial to keep in mind that cross-sections influence the experimental spectra. These cross-sections can be estimated by considering various levels' character or atomic orbital composition, and their dependence on photon energy is a key factor. For instance, at the photon energies used here, the spectra will exhibit a significant contribution from lighter elements such as C and N. In contrast, such contributions could almost be neglected at higher energies in the experimental spectrum[Ref. S6]. Br in the present case has no indication of large fraction in core level (Table S1). Before discussion for the obtained VB spectra from five conditions of post-annealing conditions, we recognized significant differences between these VB spectra in the region marked "T" at around 7 eV (Fig. S14) and "R" region (Fig. S14) from VB maximum (VBM) at 1.5 to about 4.5 eV comparing to the previous investigation for the surface of caesium doped $FAPbI_3$ single crystal[Ref. S5]. The single crystal had not indicated a strong spectrum at T and gently increased slop of spectrum in region "R". This linearly increased slope in the "R" region mostly can appear in presence of a large fraction (over 70%) of Br substituted $APbI_3$ (A: FA, FA^+, NH_3, NH_4^+, HCN and $HCNH^+$, etc.) as reported in previous investigations[Refs. S7, 8]. A $S0_m$, a relatively large fraction of Br and unknown organic impurities occur segregated at grain/domain boundaries in the surface region of MHP_m film[Ref. S9] based on observing very smooth surface morphology of MHP_m film at $S0_m$ (Fig. 1(a)). The segregated Br is in good agreement with the result of a higher Br fraction at $S0_m$ and $S1_m$ in Figs. 2(a,c) than at $S4_m$. Conversely, it is hard to define the marked T and the effects of by-products substituted in $FAPbI_3$ in this stage.

Content S4. Defect formation influenced to PSC in degraded MHP_m

Based on the analysis of GIWAXD and PES, the influence of by-products with Br^- in MHP_m film can be categorized in fitting photoluminescence (PL) spectra (Fig. S18 and Table S2). The PL tendencies of polar distorted $APbI_3$ grains (PDG)[Ref. S10] in MHP_m film are summarized in comparison with those of the non-polar $APbI_3$ grains (NPDG) in Content Fig. S1(a). We observe an overall gradual increase in the fraction of PL originating from the PDG

component from $S0_m$ to $S4_m$ caused by increasing the population of DBP substituted in MHP_m film. An increased fraction of the PDGs in MHP_m film can lead to larger instability of MHP_m film due to defects and dangling bonds, typically associated with the lone pairs of Pb in largely distorted octahedrons[Ref. S10]. A similar trend of defect formations in MHP_m film is observed in the calculation of total effective charge recombination lifetimes (τ_{eff}) by time-resolved PL as summarized in Content Fig. S1b. The τ_{eff} values are overall reduced from $S0_m$ to $S4_m$ and that can be attributed to the increased number of IPDs and H defects in the MHP_m grains as indicated by the tendency towards forming δ-$FAPbI_3$ in Fig. 1(c1). Fortunately, adding a minor fraction of Br^- in MHP_m film is expected to prevent the generation of IPDs through retained protonation of organoammonium cations.

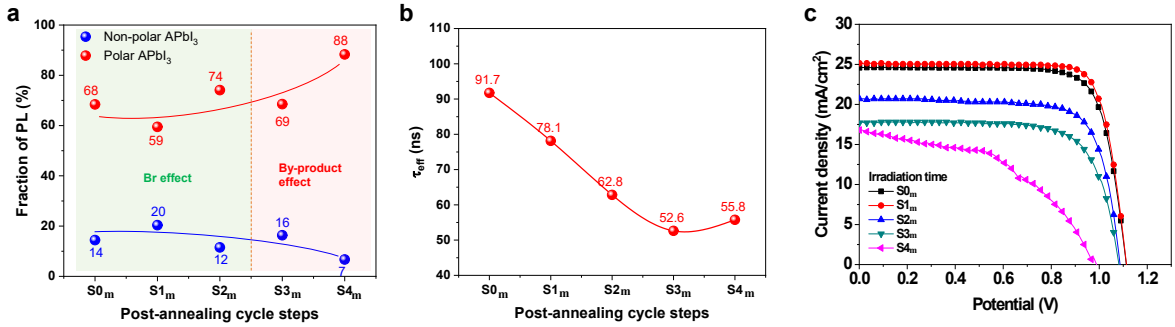

Content Figure S1. Schematic representation of IPD generation through the expected degradation pathway of FA^+ in MHP_m film. a, Summary of the effective percent fraction of photoluminescence (PL) for polar $FAPbI_3$ after various post-annealing cycles, based on the PL spectra in Fig. S18 and Table S2. **b,** the obtained effective total charge recombination (τ_{eff}) are summarized based on the results of fitting parameters in Fig. S19. **c,** Measured J-V curves from five PSCs fabricated under five different post-annealing conditions (without AR and PEAI treatment). Solar cell parameters are summarized in Table S3.

The performance of each post-annealed MHP_m film in the fabricated PSCs is evaluated based on their photo-to-power conversion efficiencies (PCEs), which are summarized in Content Fig. S1(c) and Table S3. PCE of the $S1_m$ exhibits 1.3% higher than the $S0_m$ due to the segregated Br onto the surface of MHP_m film (Figs. 2(a,c)). However, both exhibit a decline from the $S2_m$ to the $S4_m$. Notably, the PSC of the $S4_m$ clearly shows the PSC's low fill factor (FF) compared to the other four PSCs.

Content S5. Mechanism of VBs formation in degraded MHP_m

Based on the aforementioned analysis results, the significant changes in crystal morphology of MHP_m film seem to be influenced by the presence of deprotonated by-product

(DBP), resulting in a large fraction of the vaporized Br_2 and HBr after the $S2_m$. Interestingly, in the $S0_m$ and $S1_m$, despite the existence of a certain fraction of protonated by-product (PBP) occupying at A site along with a significant presence of FA^+ and a very small fraction of MA^+, consistent with prior work[Refs. S11, 12], the d-spacings for α(100) and α(200) in MHP_m film remain relatively well-preserved. One reason that can potentially complementarily contribute to the preservation of the (quasi-)cubic $APbI_3$ framework is the occupied fraction of comparatively small DBPs. Furthermore, the doped Br^- in the MHP_m film plays a role in assisting the retainment of these lattice parameters, according to Zheng et al.[Ref. S13]. Probably, the added tiny fraction of Br^- in the lattice distance of (111) plane of α-$FAPbI_3$ domain/grain interiors leads to stabilize the MHP_m film with releasing and balancing crystal strain. This evidence is supported by changes observed in ε_{wh} for the sum of the surface and full-depth conditions (Fig. S6(b)). Furthermore, we have recognised the migration of Br from the interface near the ETL to the surface of the MHP_m film. From $S2_m$ to the $S4_m$, it is impossible to retain lattice parameters due to largely increased fraction of DBPs with vaporized Br_2 and HBr. Additionally, a substantial portion of DBPs (as marked 'M_p') is observed within this $APbI_3$ framework, as indicated in the N 1s spectra of the $S4_m$ in Fig. 2(c). This presence also correlates with a noticeable expansion in the d-spacing of α(200), as shown by-products in Figs. 1(e,f). In particular, the dissociated H^+ (as free protons) in MHP_m film can migrate and interact with the DBP at the A site. This deprotonation occurs via the partially ionized major I^- and minor Br^- in the MHP_m film. Despite the migration of the doped Br^- in MHP_m film, it can be a trigger to prevent ionization and fragmentation of FA^+ in accelerating the vaporization process of I^-, Br^- and FA^+. If the minor fraction of Cl^- has doped in MHP_m film, it acts as the likely doped Br^- but has a larger effect to prevent degradation of MHP_m film under slower migration velocity of Cl^-[Ref. S14] and a higher proton affinity than Br^-[Ref. S15] than Br^-. Furthermore, if the crystal lattices of α(100) and α(200) are affected by the added Br^-, d-spacings of α(100) for the $S2_m$ at two depth conditions should follow the inversion proportional trend of fraction changes in Br/Pb on MHP_m film in Fig. 2(a). However, it has not appeared at the changing d-spaces of α(100) for $S3_m$ and $S4_m$ in particular.

This degradation of FA^+ from $S2_m$ may be affected by the migration and the dissociation of the Br^- and I^- compositions (Figs. 2(a,c)). Notably, Br^- possesses higher proton affinity than I^- [Ref. S15]. Therefore, we can consider two types of charge transfer mechanisms under heating or radiation conditions, or when both are combined: 1) $Br^-\cdots I^+\cdots 2e^-$ and 2) $Br^-\cdots I^{\bullet(radical)}\cdots e^-$.

Subsequently, the halides dissociate from PbX_2 (X: I and Br) and organoammonium halide. In the first case, the generated $2e^-$ can contribute to neutralize charge of Pb^{2+} (Pb^0) and then occurs vaporization process. In the second case, the e^- can contribute to neutralize charges of H_2N-CH-NH_2 and finally dissociate into H_2N-CH-NH and $H^{+(\bullet)}\cdots I^{-(\bullet)}$. At the outset of the degradation of an organoammonium cation, deprotonation on the ammonium site is the initial step, leading to a further dissociation of the molecule over the temperature range of its thermodynamic stability limit[Refs. S16-20]. This initial dissociation process can accelerate the fragmentation process of FA^+ to NH_3 and HCN under the reduced fraction of Br.

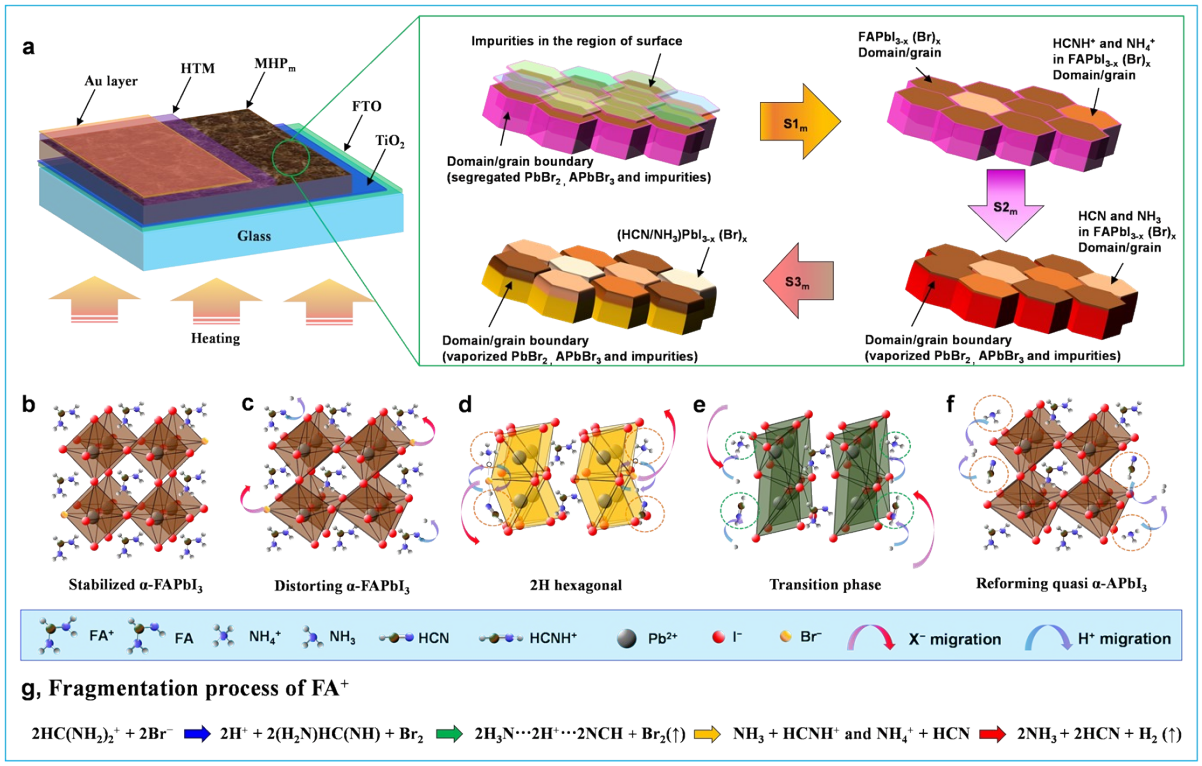

Content Figure S2. Schematic representation of IPD generation through the expected degradation pathway of FA^+ in MHP_m film. a, Overview of the degradation process within grain/domain of MHP_m film. The color gradient (from dark red to red) of the thick arrow corresponds to the predicted penetration depth of Br in the surface region (10 nm depth) based on the results of XPS investigation. In the green coloured solid line box, the process of the degraded MHP_m film are schemed. The surface of MHP_m film at $S0_m$ has contaminated by large impurities. The impurities are consisting of residual organics, un-incorporated A site cations (including by-products) and metal halides. The large fraction of the impurities is vaporized after the $S1_m$. From $S2_m$ to $S4_m$, Br is rapidly vaporized and producing the large fraction of by-products in the surface region and deeper depth of MHP film. DBP substituted $FAPbI_{3-x}Br_x$, $HCNPbI_{3-x}Br_x$ and $NH_3PbI_{3-x}Br_x$ are referred to polar distorted grain/domain. Detailed degradation of grain/domain is described by four model MHP_m frameworks: **b,** Ideal $FAPbI_3$ framework, **c,** Thermal distortion of $FAPbI_3$ involving deprotonation of FA^+, **d,** Degradation leading to IPD (2H hexagonal) facilitated by $NH_3\cdots H^+\cdots CNH$ as an intermediate complex, **e,**

Re-stabilization leading to transition phase with NH_4^+, $HCNH^+$, FA^+ and FA and **f,** Re-formation of quasi-α-$APbI_3$ with NH_3, HCN, FA^+, and FA. (adapted with permission from Ref. S21) **g,** Illustration depicting the fragmentation process of FA^+.

In this regard, the degradation of local MHP_m grain is proposed in schemes in Content Fig. S2. Firstly, the dominant $FAPbI_3$ with tiny quantities of DBP and PBP substituted $FAPbI_3$ are formed at the $S0_m$. The population of DBP and PBP substituted $FAPbI_3$ domains in MHP_m increases at the $S1_m$ and $S2_m$. From $S3_m$, DBP substituted $FAPbI_3$ can be fully degraded into $(HCN/NH_3)PbI_3$. In Content Figs. S2(b-f), it schemes the formation of IPD and recrystallization process along with the fragmentation of FA^+. In the initial stage, as the stabilized α-$FAPbI_3$ (Content Fig. S2(b)), this α-$FAPbI_3$ is distorted by thermally induced deprotonation of FA^+ to neutral FA with the migration of Br^- coupling H^+ as described in Content Fig. S2(c). We proposed that the degradation process begins with the partial fraction of $FA\cdots H^+$ in the metal halide framework, transforming into $NH_3\cdots H^+\cdots NCH$ as an intermediate complex, which further deforms into IPD, as depicted in Content Fig. S2(d). This intermediated by-product molecule can be further degraded by light[Ref. S22] and heating[Ref. S23] conditions again. The IPD, in conjunction with $NH_3\cdots H^+\cdots NCH$, proceeds to undergo complete fragmentation of $NH_3/HNCH^+$ or NH_4^+/NCH during the transition phase, as shown in Content Fig. S2(e). Indeed, the presence of free H^+ in the MHP_m film creates relatively unstable conditions that readily interact with the lone pairs of Pb within the significantly distorted octahedrons[Refs. S10, 24, 25]. Simultaneously, halide-bonded Pb may dissociate due to the existence of free H (mostly H^- ions by electron transfer from free halide), causing halides to migrate. Consequently, α-$FAPbI_3$ partially transforms into PbI_2 via the δ-phase. This transformation is supported by the highest fractions of PbI_2 and δ-$FAPbI_3$ observed during the $S3_m$ (Fig. 1(d)). Content Fig. S2(f) illustrates the complete vaporization of H^+ ions from the MHP_m film, resulting in more contracted lattices due to the distortion caused by the abundance of deprotonated by-product molecules within the reformed quasi-α-$APbI_3$ framework. Upon the overall observation, comparing the behavior of organoammonium cations and varying halide concentrations, the fragmentation process of FA^+ in Content Fig. S2(g) can be somewhat hindered by the higher proton affinity of the doped Br^-(or/and Cl^-)[Ref. S15] than that of I^- in the MHP_m film. This condition is highly susceptible to heating and radiation conditions, facilitating halide dissociation and migration of by-products under applied continuous external stresses. When NH_4^+ and NH_3 are substituted in $FAPbI_3$ in particular, we can draw insights from previous reports where doping tiny size of non-polar molecules such as NH_4^+ in $FAPbI_3$ has been

observed to induce ferroelectricity[Ref. S26]. Similarly, we presume that the presence of $HCNH^+$ in $FAPbI_3$ may serve a similar role to substituted NH_4^+. However, unlike the cases of methylammonium (which induces ferroelectric tetragonal structure) and methylamine (displaying paraelectric properties similar to cubic) within $APbI_3$ frames[Ref. S27], the DBP in $FAPbI_3$ probably does not contribute to polar ferroelectric stabilization.

Supplemental data

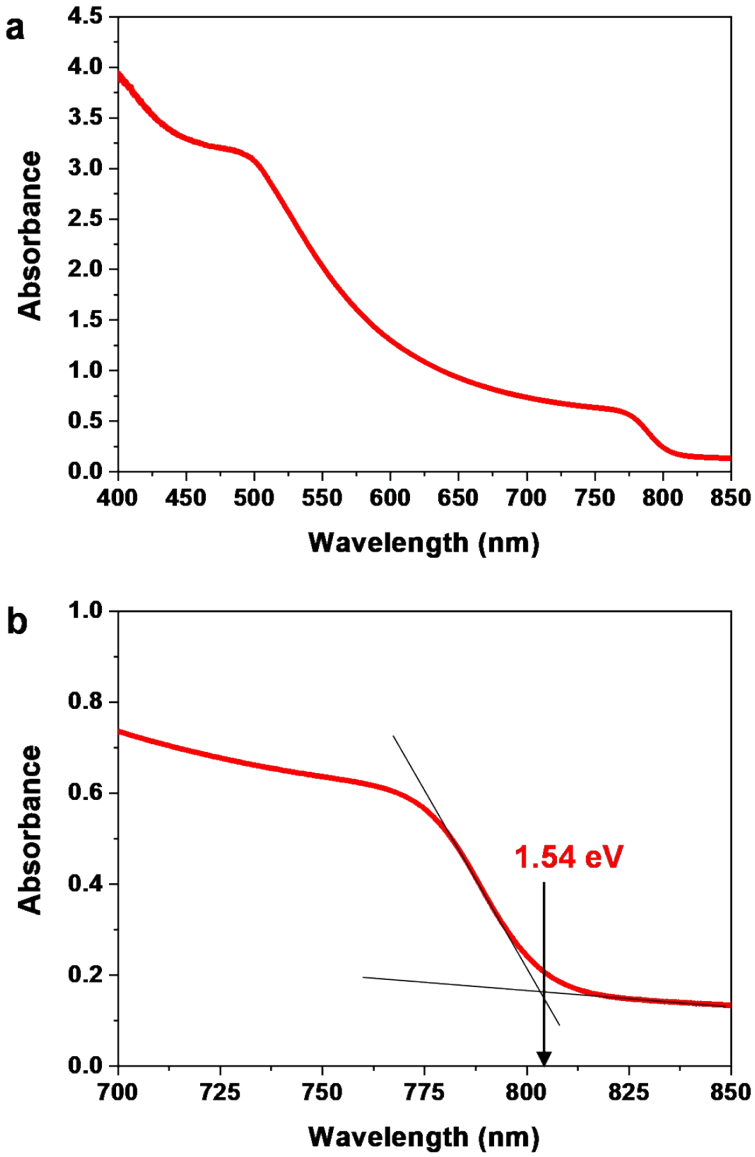

Figure S1. UV-vis spectra. UV-vis spectrum of post-annealed MHP_m film for **a,** full, and **b,** the magnified spectrum in the range of 700−850 nm.

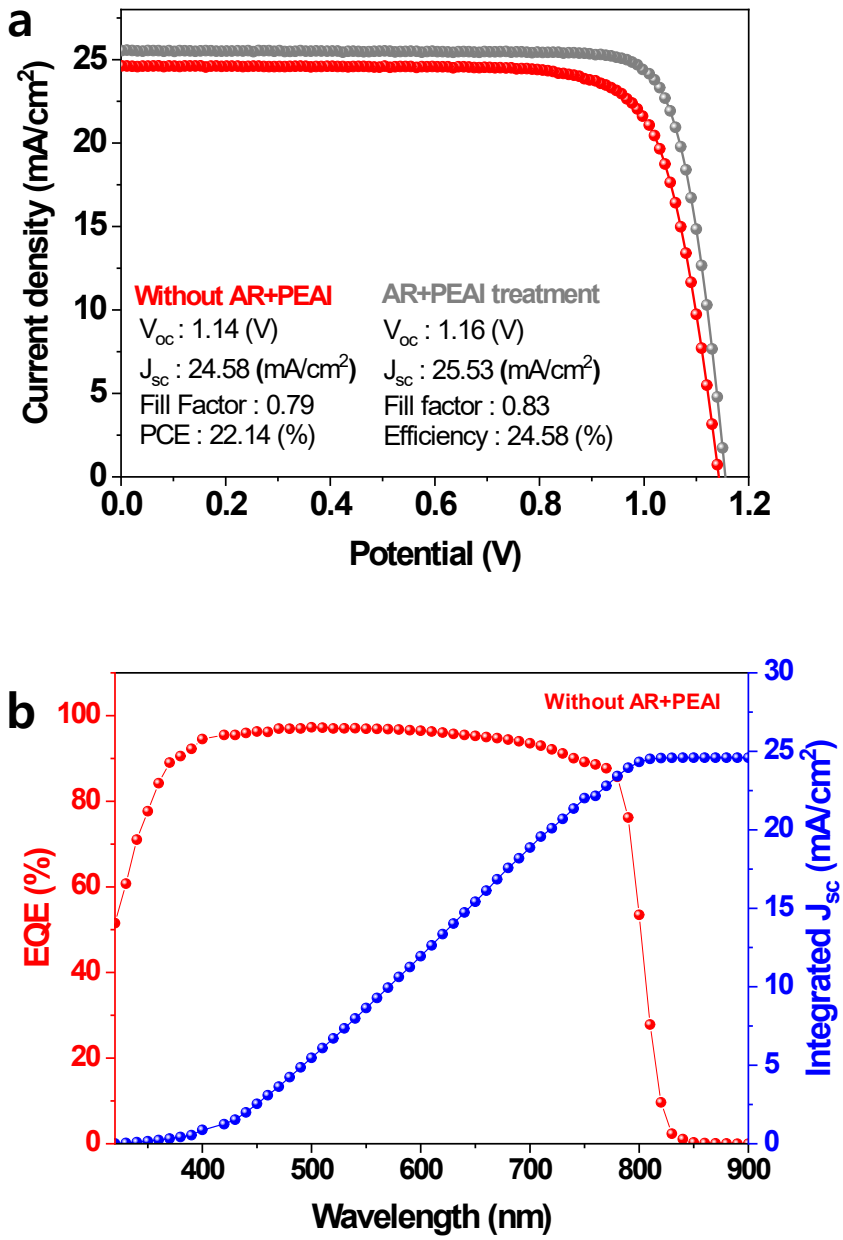

Figure S2. Solar cell performance for monitoring the decomposition process of model metal halide perovskite (MHP_m) thin film. a, J-V curves of PSCs evaluated under conditions with/without phenethylamine hydriodide (PEAI) passivation between MHP_m film and hole transfer layer. **b,** Corresponding EQE curves with integrated photo-current density. The MHP_m-based PSC achieved 24.58 % PCE with anti-reflection (AR) film and phenethylammonium iodide (PEAI) treatment (22.14 % without AR film and PEAI treatment). (The detailed fabrication method of PSC is described in the section on method.) The corresponding external quantum efficiency (EQE) from this PSC (without AR film and PEAI treatment) reached 96.94 % at a wavelength of 550 nm. The integrated photo-current density was 24.60 $mAcm^{-2}$, in good agreement with the short-circuit current density (J_{sc}).

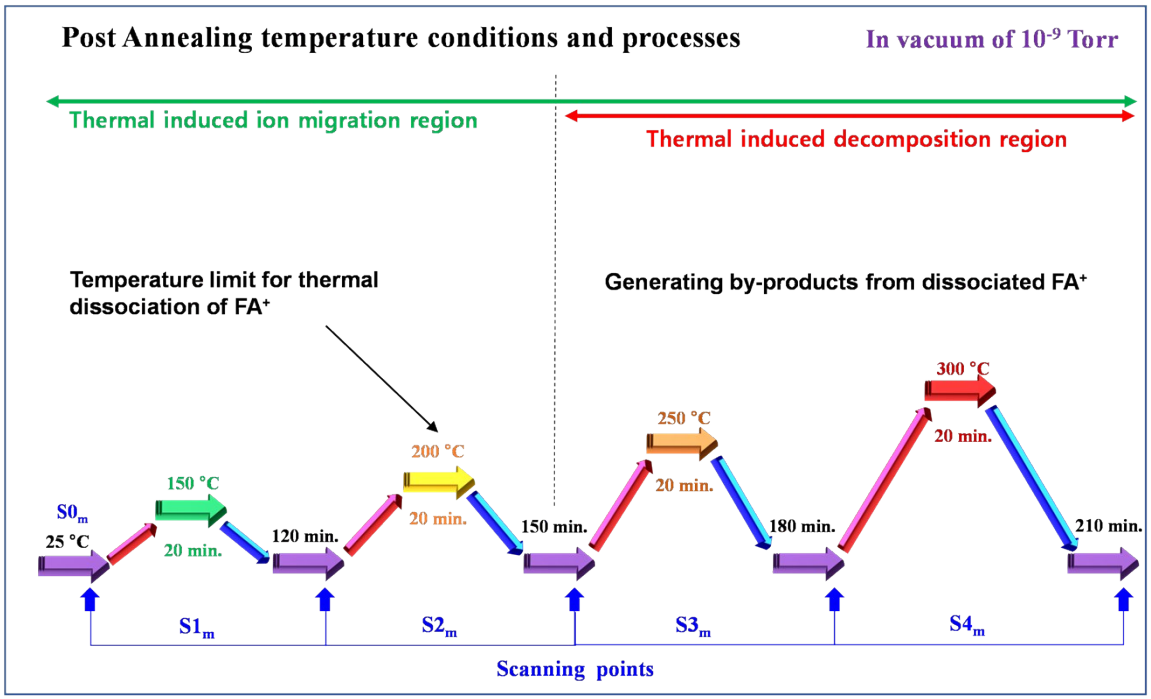

Figure S3. Post-annealing cycle steps for thermal degradation of MHP_m film. Post-annealing steps, denoting their respective temperatures and durations. The scanning points are marked at blue coloured arrows after the temperature stabilization at 25 °C. The degradation of the MHP_m films was studied in a vacuum chamber at 10^{-9} Torr, with post-annealing carried out over a period of time during temperature rise, and to prevent the formation of reactive gases in humid air conditions. The post-annealing process of the MHP_m film involved five cycles (denoted as $S0_m$, $S1_m$, $S2_m$, $S3_m$ and $S4_m$, respectively), each consisting of heating for 20 min. and cooling, followed by a stabilization time. The analysis of the process is divided into two distinct temperature regions: the first encompassing ion migration occurring within the temperature range of 25 °C to 200 °C, and the second focusing on degradation observed in the temperature range of 200 °C to 300 °C. This categorization was motivated by the previously reported thermal degradation temperature of $FAPbI_3$[Refs. S18, 28] and the thermal stability threshold of FAI at ~200 °C[Ref. S11]. For removing impurities onto MHP_m film during post-annealing process, we set a vacuum condition of 10^{-9} Torr. This post-annealing condition is selected due to the accelerating degradation of MHP_m film under the consideration of testing PSCs in extreme environmental out-door field condition.

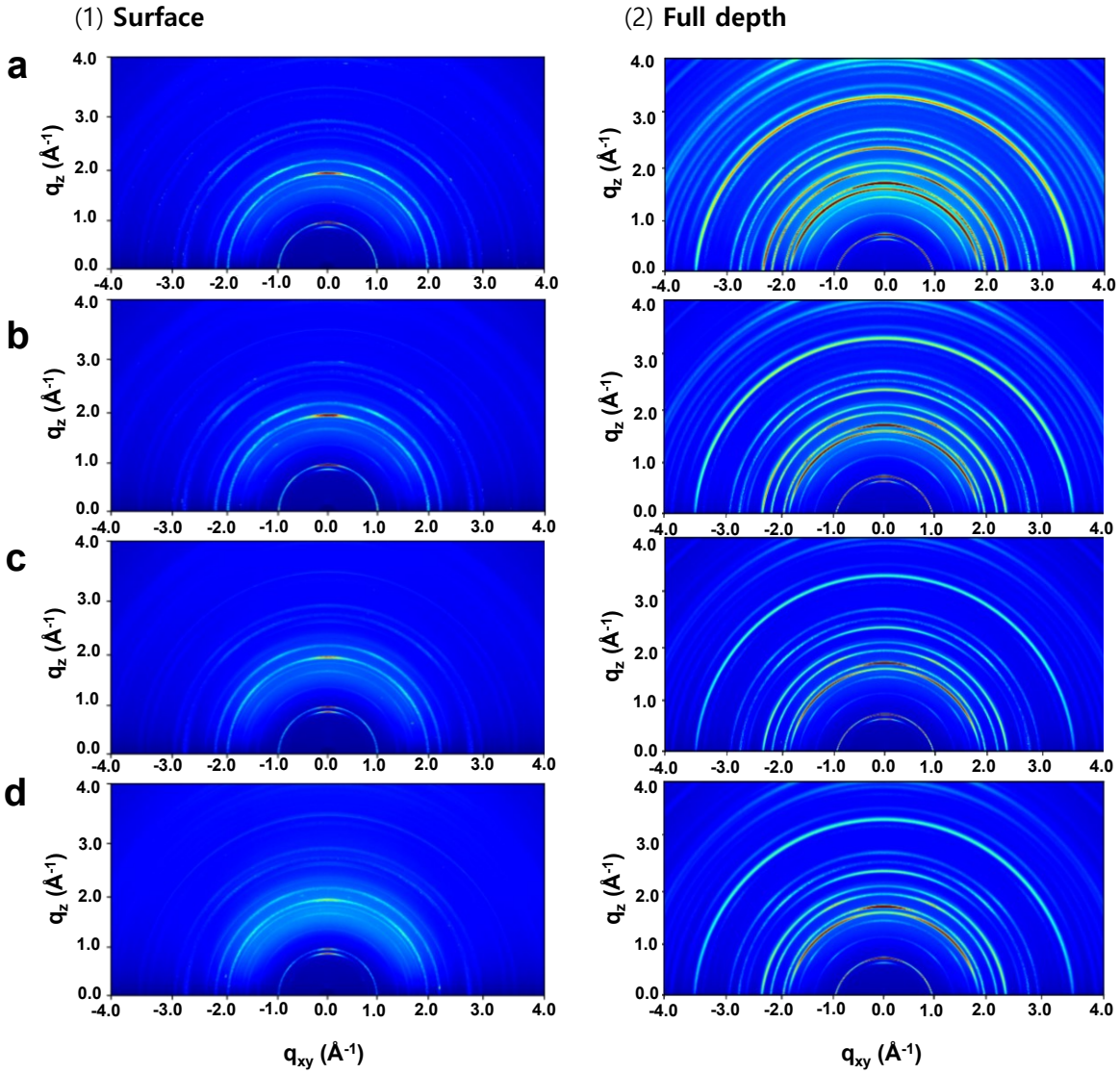

Figure 4. GIWAXD investigations. The monitored 2D-GIWAXD images of MHP_m at depths of **1,** 10 nm depth and **2,** full depth for **a,** $S1_m$, **b,** $S2_m$, **c,** $S3_m$, and **d,** $S4_m$ steps.

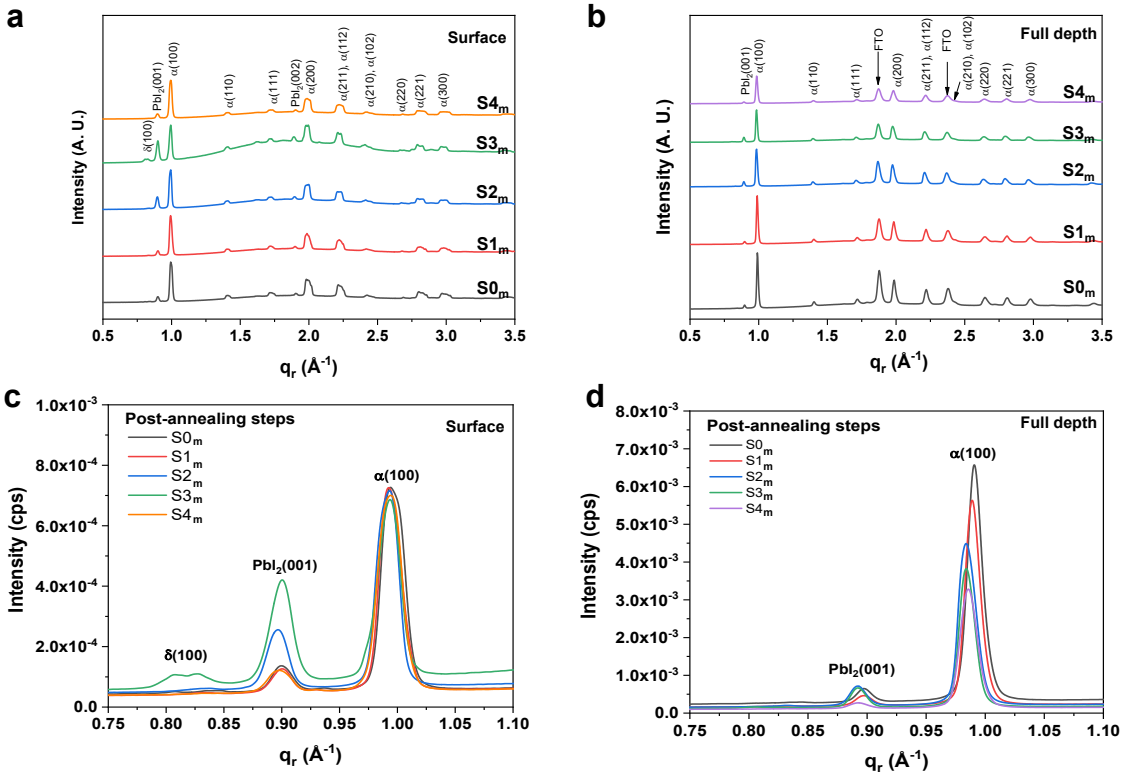

Figure S5. GIWAXD investigations. The azimuthal angular average full 1D-GIWAXD profiles of $S0_m$, $S1_m$, $S2_m$, $S3_m$ and $S4_m$ at two MHP_m film depth conditions at **a,** 10 nm depth (X-ray incidence angle of 0.117°) and **b,** full depth (0.8°) are converted from 2D-GIWAXD images (Fig. S4). The magnified 1D-GIWAXD profiles are displayed at **c,** 10 nm and **d,** full depths. The calculation of MHP_m film depth with X-ray incidence angles are referred to previous investigation[Ref. S29].

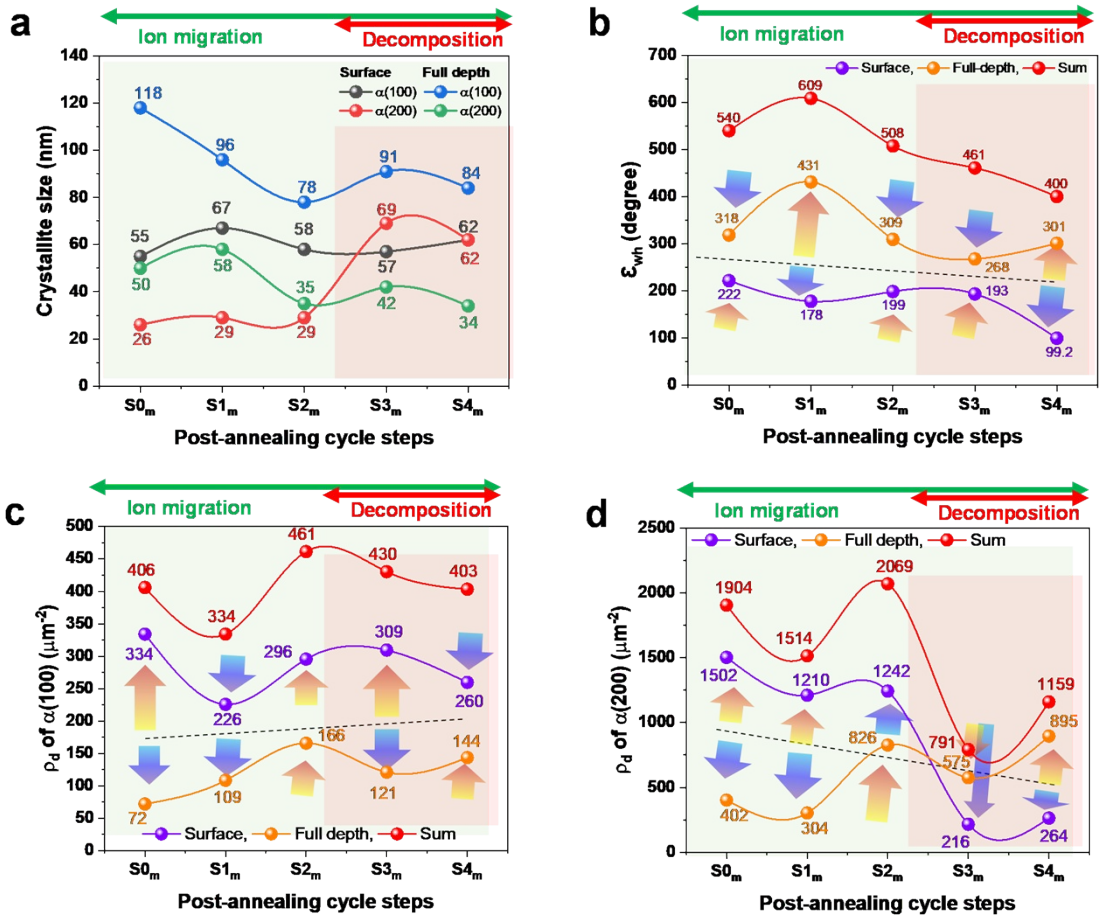

Figure S6. Calculations of crystallite size, microstrain (ε_{wh}) and dislocation density (ρ_d) . At two depth profiles, the calculated **a,** crystallite size (using Scherrer Formula: $L = (0.94\times\lambda)/(FWHM/Cos\ \theta)$[Ref. S30], L :crystallite size, λ : the incident X-ray wavelength, FWHM : the full width of half maximum, and θ : Bragg angle) **b,** ε_{wh} and **b,c,** ρ_d are displayed. ε_{wh} is obtained from Williamson hall plots in Figs. S7 and S8. The obtained ε_{wh} values denote compressive strain condition[Ref. S15]. ε_{wh} on MHP_m film is determined using an equation $\varepsilon_{wh} = \beta/(4\tan\theta)$[Ref. S31] (β: full width and half maximum of peaks at α (100) and α(200)). ρ_d is calculated using a formula of Williamson and Smallman: $\rho_d = 1/D^2$ (D: crystallite size)[Ref. S32]. In this calculation of ρ_d, Burgers vector is not considered. The resulting sums obtained from the two depth conditions represent relative values used to track tendencies.

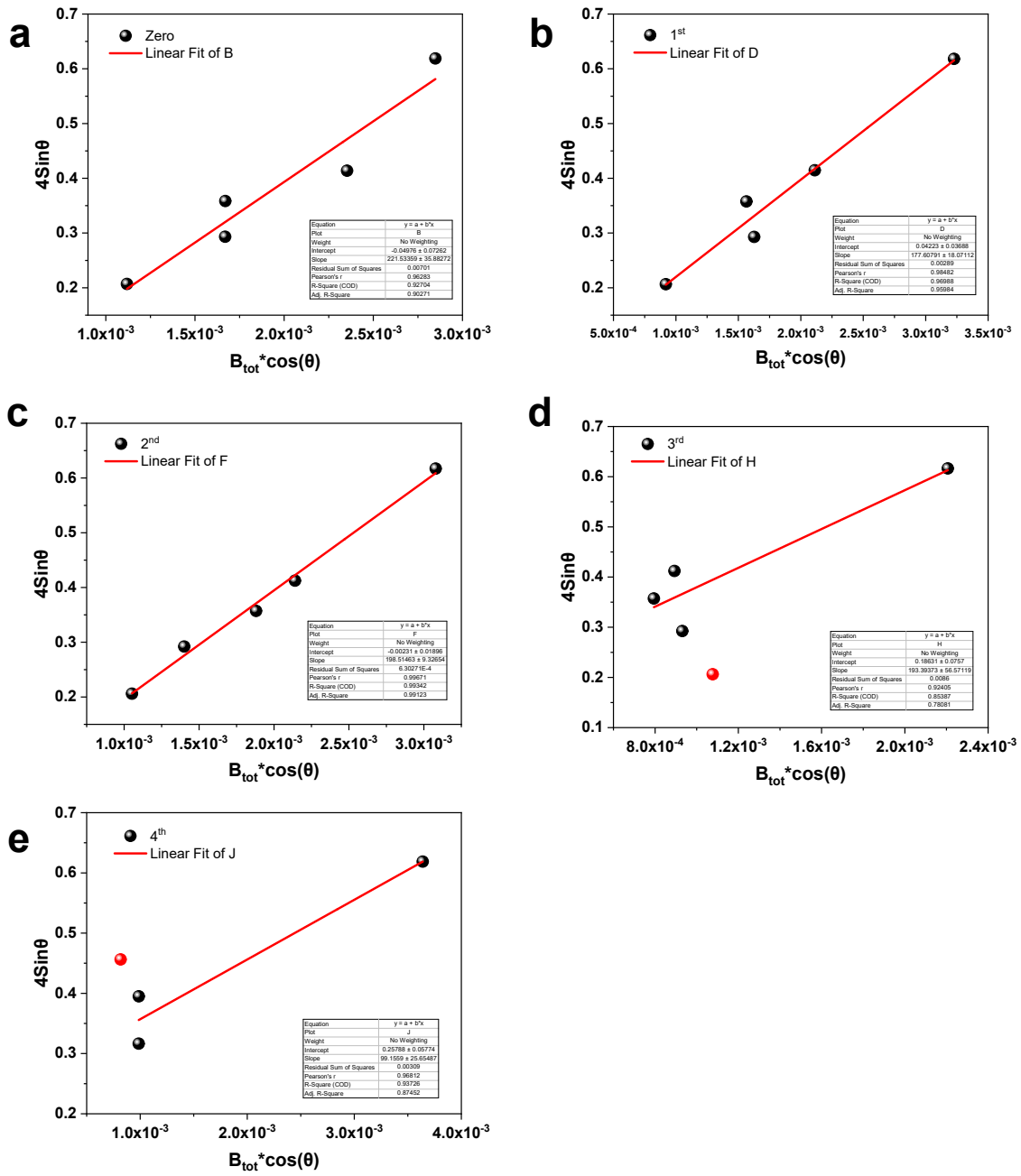

Figure S7. Micro-strains of Surface on MHP_m film. Williamson Hall plots are displayed for The **a,** $S0_m$, **b,** $S1_m$, **c,** $S2_m$, **d,** $S3_m$ and **e,** $S4_m$ steps.

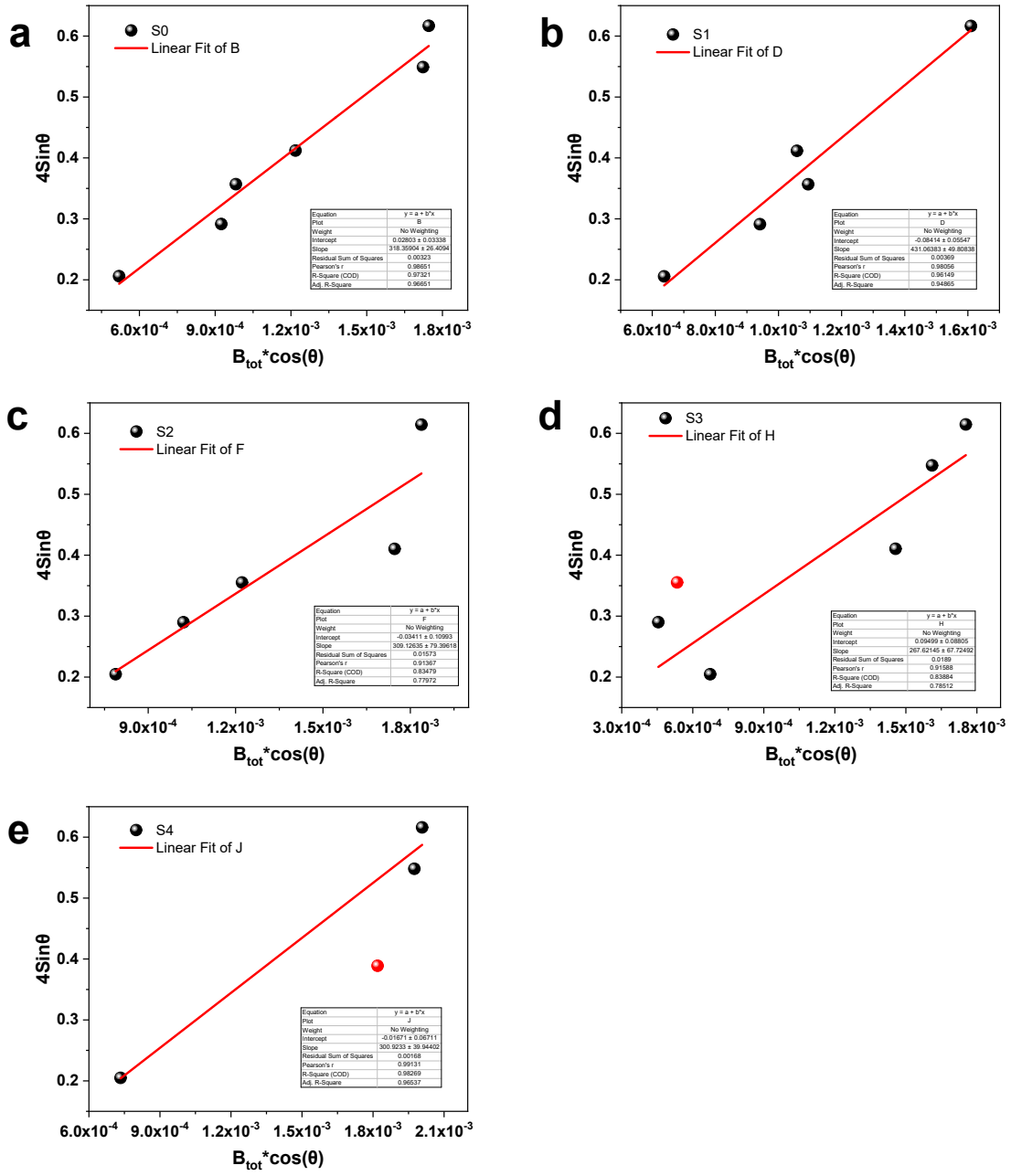

Figure S8. Micro-strains of full depth MHP_m film. Williamson Hall plots are displayed for The **a,** $S0_m$, **b,** $S1_m$, **c,** $S2_m$, **d,** $S3_m$ and **e,** $S4_m$ steps.

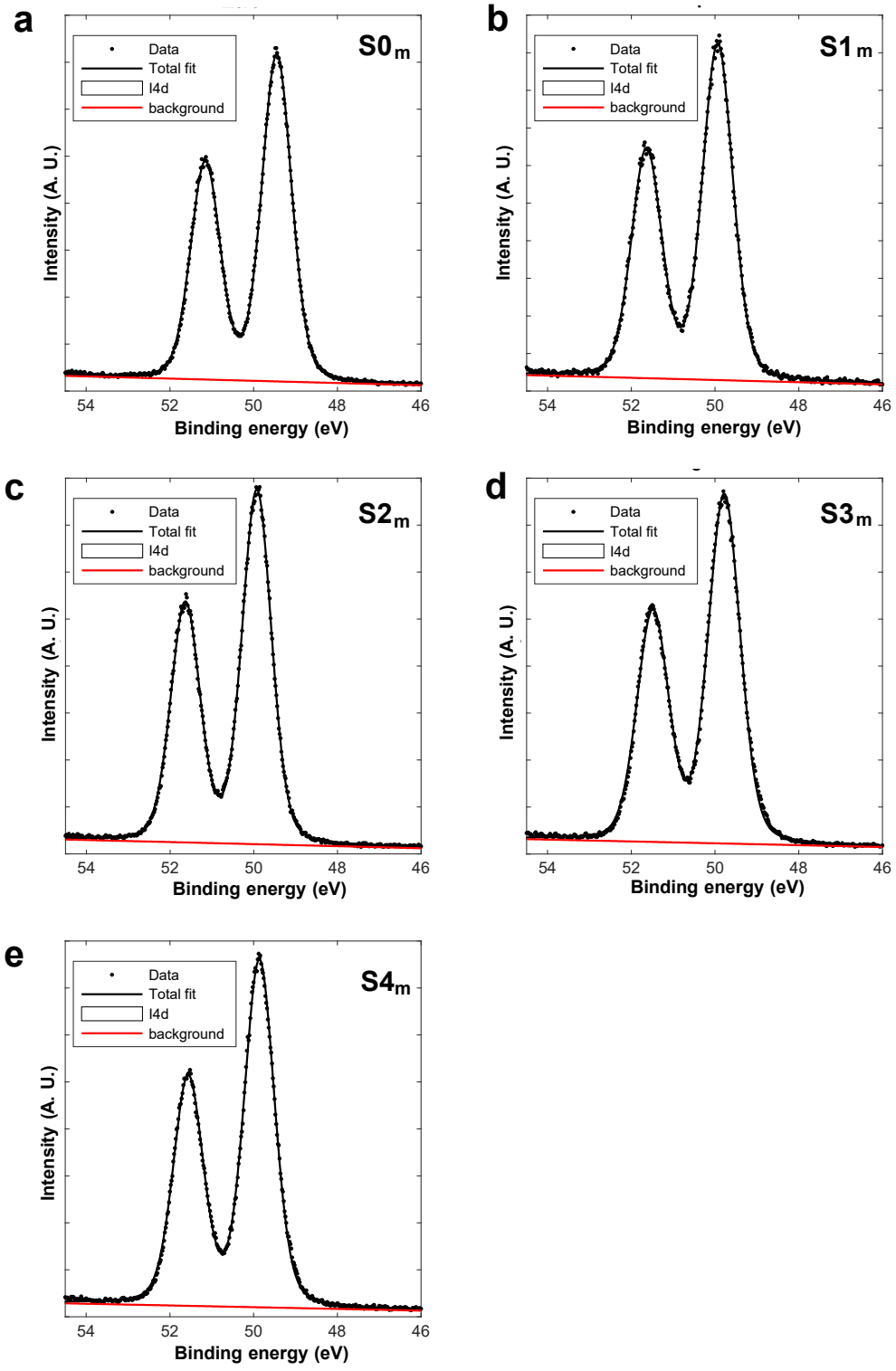

Figure S9. PES analysis in I 4d spectra. The **a,** $S0_m$, **b,** $S1_m$, **c,** $S2_m$, **d,** $S3_m$ and **e,** $S4_m$ steps of MHP_m films were scanned in I 4d spectra and corresponding fit spectra. I 4d spectra energy calibrated to Pb $4f_{7/2}$ "$S0_m$" and normalised to Pb $4f_{7/2}$ (Pb^{2+}) intensity.

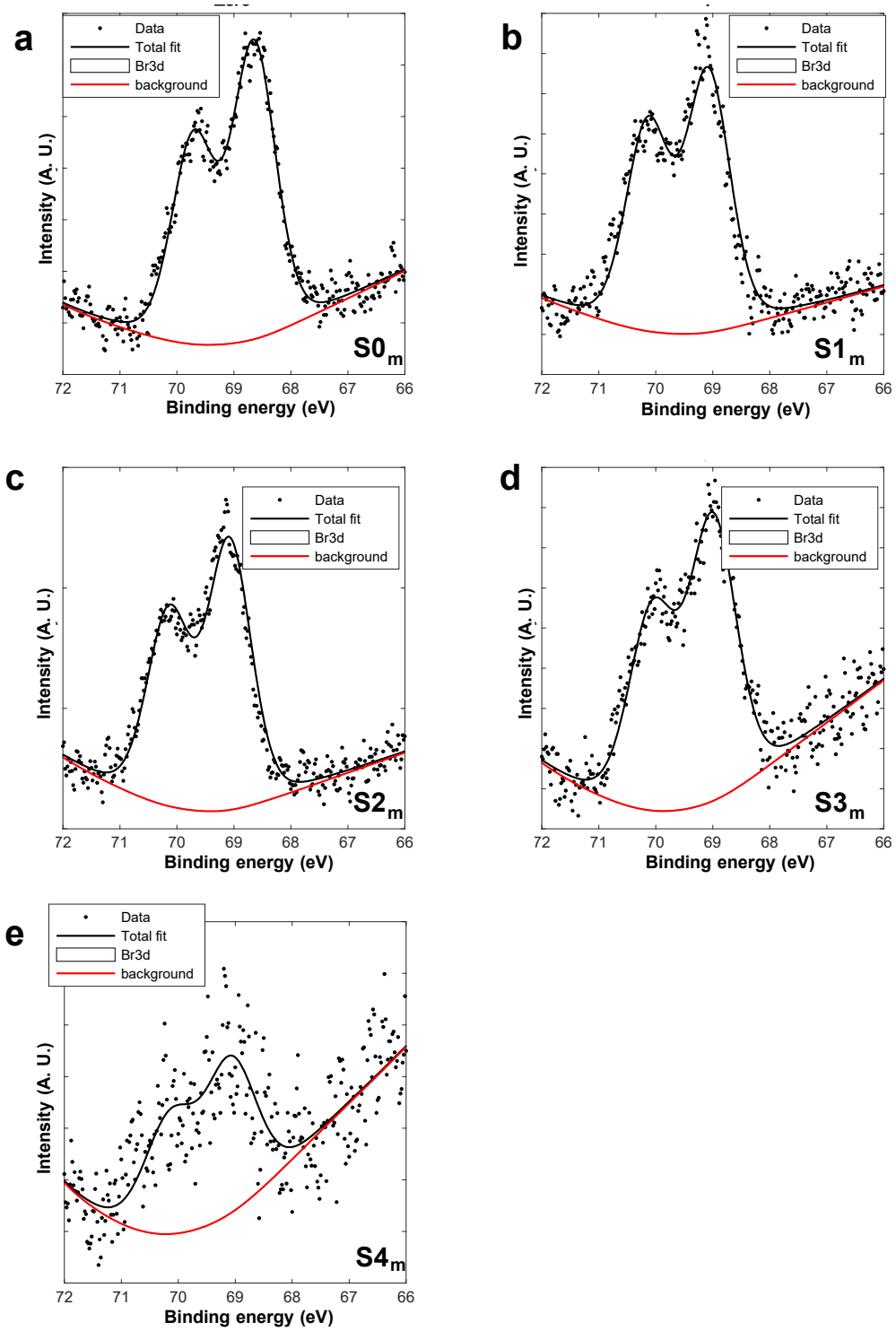

Figure S10. PES analysis in Br 3d spectra. The **a,** $S0_m$, **b,** $S1_m$, **c,** $S2_m$, **d,** $S3_m$ and **e,** $S4_m$ steps of MHP_m films were scanned in I 4d spectra and corresponding fit spectra. Br 3d spectra energy calibrated to Pb $4f_{7/2}$ "$S0_m$" and normalised to Pb $4f_{7/2}$ (Pb^{2+}) intensity.

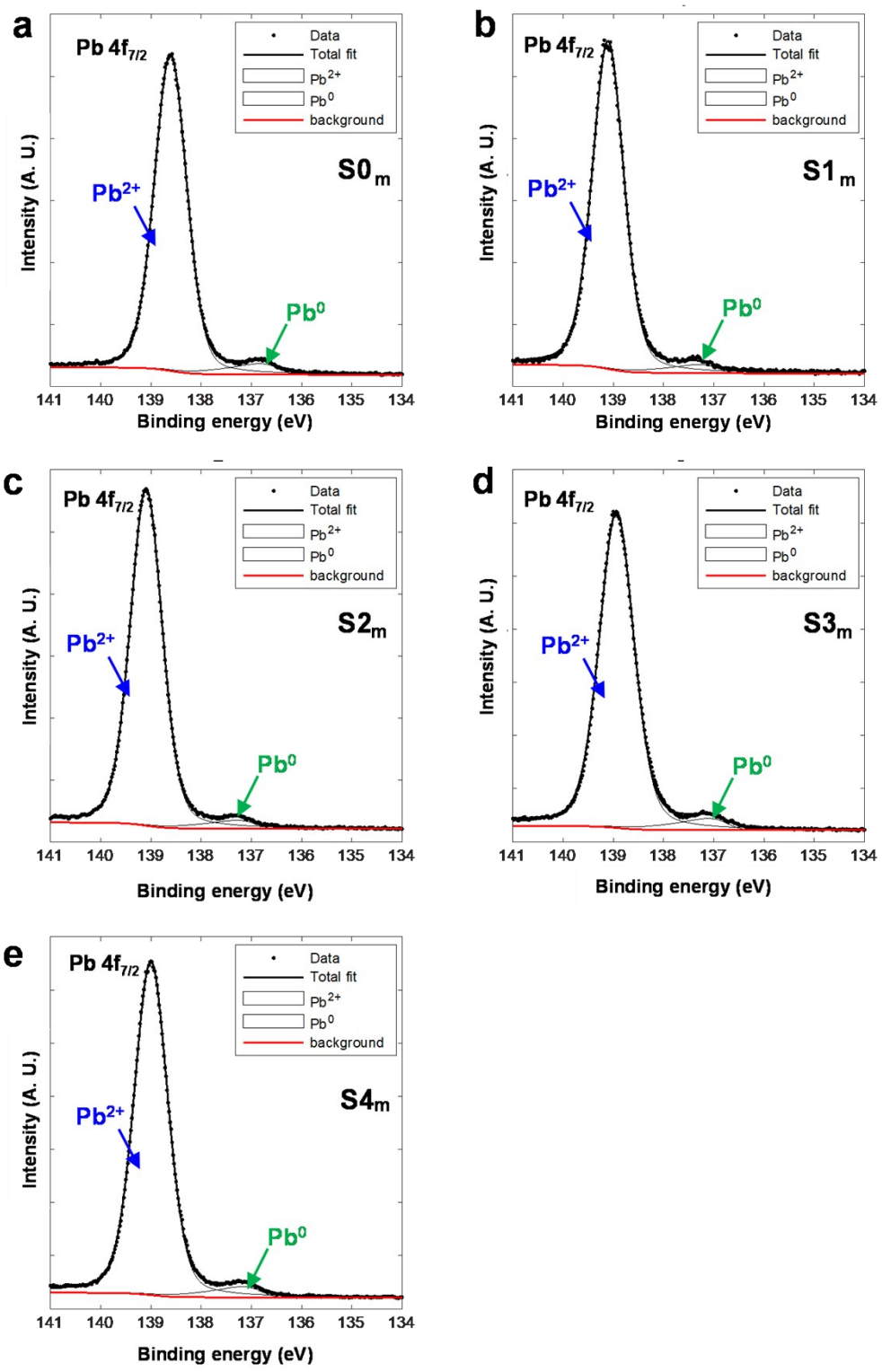

Figure S11. PES analysis in Pb $4f_{7/2}$ spectra. The deconvoluted Pb $4f_{7/2}$ spectra and corresponding fit spectra are summarized for five post-annealing conditions of The **a,** $S0_m$, **b,** $S1_m$, **c,** $S2_m$, **d,** $S3_m$ and **e,** $S4_m$ steps. All spectra were deconvoluted using Voigt function,[Ref. S33] defining two components noted as Pb^{2+} and Pb^0. **f,** Pb 4f spectra are energy calibrated to Pb $4f_{7/2}$ "$S0_m$" and normalised to Pb $4f_{7/2}$ (Pb^{2+}) intensity.

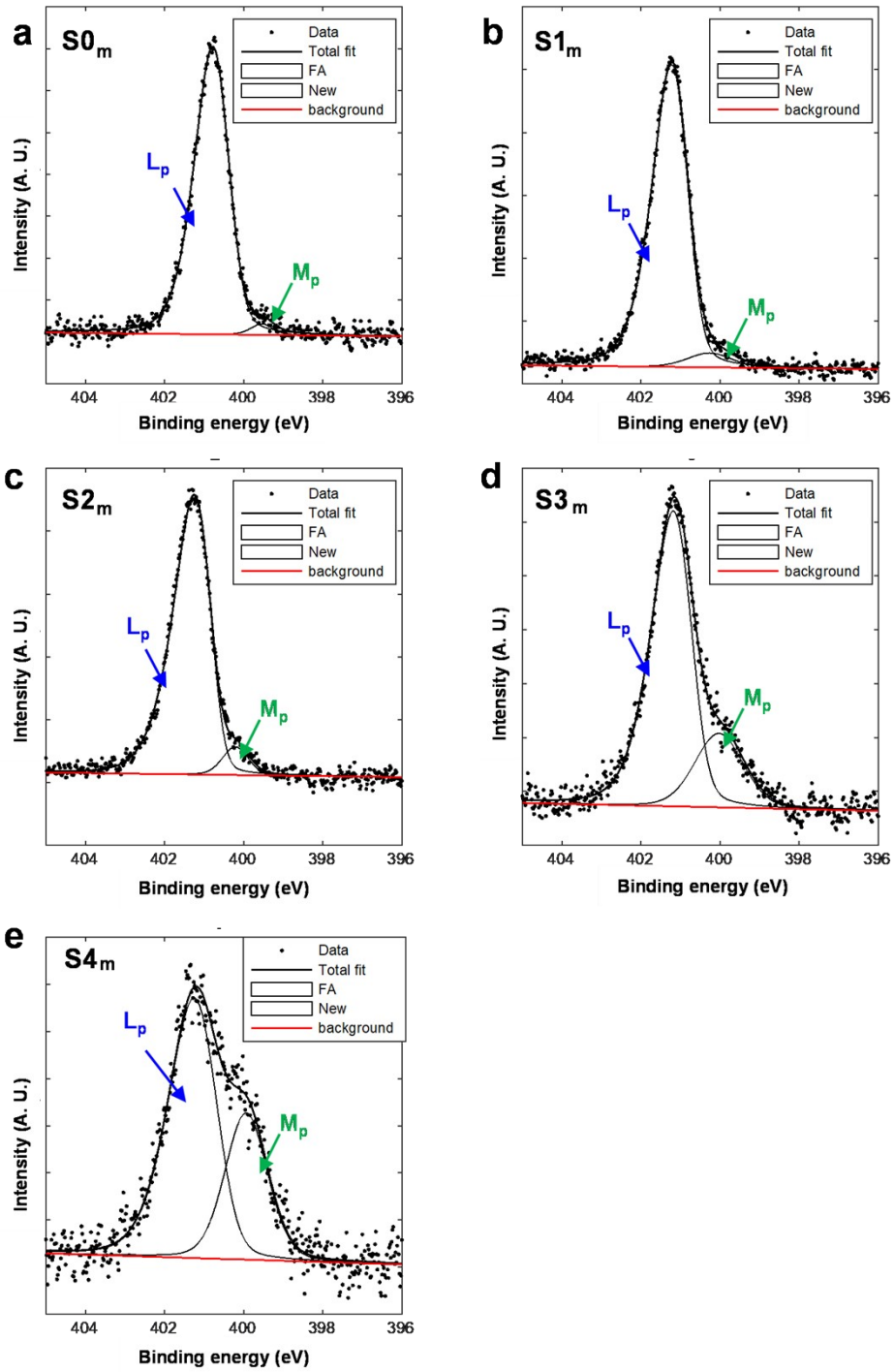

Figure S12. PES analysis in N 1s spectra. The **a,** $S0_m$, **b,** $S1_m$, **c,** $S2_m$, **d,** $S3_m$ and **e,** $S4_m$ conditions of MHP_m films were scanned in N 1s spectra. All spectra were deconvoluted using Voigt function[Ref. S33], defining two components noted as L_p and M_p. N 1s spectra are energy calibrated to Pb $4f_{7/2}$ "$S0_m$" and normalised to total N 1s intensity. The corresponding chemical components with L_p and M_p are summarized with fitted parameters in Table S1.

Table S1. The analysis of PES and fitting parameters. The N 1s spectra for $S0_m$, $S1_m$, $S2_m$, $S3_m$, and $S4_m$ steps are deconvoluted as displayed in Figs. S9-S12. The deconvoluted parameters are summarized. The chemical component of L_p is referring to FA^{+}[Refs. S33, 34]. The M_p component is referring to $C{\equiv}N^{-}$[Ref. S5, 34], nitrile (-C≡N:)[Refs. S5, 35], nitrogen in an aromatic ring, N-(C=O)-[Refs. S5, 35] and Amide[Ref.s S5, 35]. Near 402 eV in N 1s refers to akylammonium and NH_4^+ in Refs. S7 and S35).

	Area ratios (proportional to concentration ratios, but not actual concentrations)			**Ratios with initial ratios set to those expected from stoichiometry**			**M_p (%)**
	I 4d /Pb 4f	Br 3d /Pb 4f (× 10)	Br 3d /I 4d (× 10)	I 4d /Pb 4f	Br 3d /Pb 4f	Br 3d /I 4d (× 10)	N 1s
$S0_m$	0.353	0.128	0.351	2.91	0.09	0.31	2.5
$S1_m$	0.365	0.145	0.397	3.01	0.11	0.35	5.3
$S2_m$	0.359	0.116	0.322	2.96	0.084	0.28	6.6
$S3_m$	0.316	0.064	0.203	2.60	0.046	0.18	22.6
$S4_m$	0.299	0.030	0.100	2.46	0.022	0.09	33.2

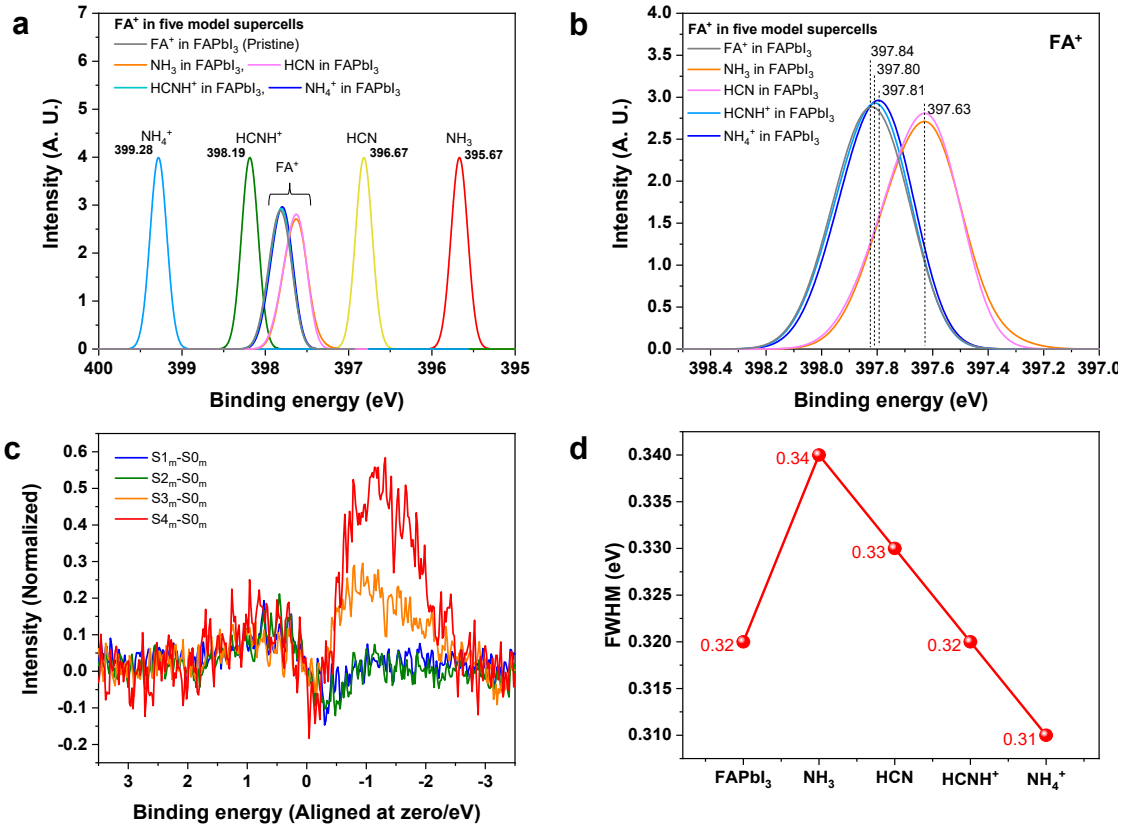

Figure S13. DOS in N 1s spectra. a, BEs for each N atom, including estimates of their average and standard deviation from four defect model systems (DMSs) and pristine $FAPbI_3$ as reference model system in Fig. 2(d). **b,** The magnified peaks in the range of 397.0−298.5 eV is displayed from figure A. The reason for shifting peaks is described in Content S1. **c,** The differential N 1s spectra are displayed in Sn_m (n : numerical number from 1 to 4) minus $S0_m$ from spectra in Fig. 2(b). **d,** The obtained FWHM in N 1s spectra of five model supercells in Fig. 2f has summarized.

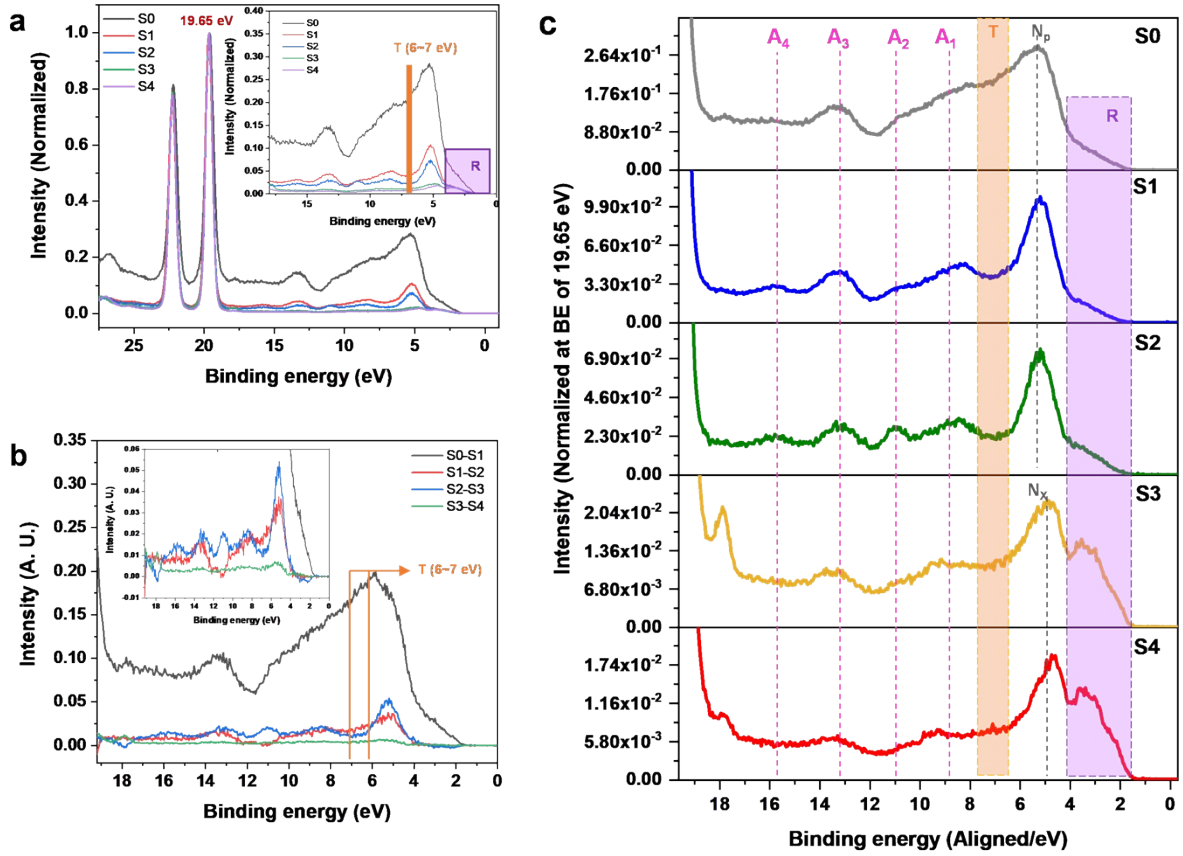

Figure S14. PES analysis in valence band (VB) spectra. a, The scanned VB spectra (0−27 eV) for S0, S1, S2, S3 and S4 conditions of MHP_m films are shown to normalize spectra at around 19.65 eV. In a satellite figure in figure a, the magnified VB spectra in the region of 0−18 eV are displayed with the marked R in the range of VB maximum (VBM) to 4.5 eV. For clearer description of vaporizing/reforming fractions of chemical components in VB region, **b,** it displays the relevant fractional changes in the range of 0−19.65 eV. The largely vaporizing chemical components in the surface region are exhibited in the range of around 4−10 eV. **c,** The magnified VB spectra for five conditions are displayed with the marked A_n (n ranging from 1 to 4.) In particular, the marked 'T' is showing unusually high intensity and the marked 'R' refers to the region from VBM to 4.5 eV that corresponds to the first VB region.

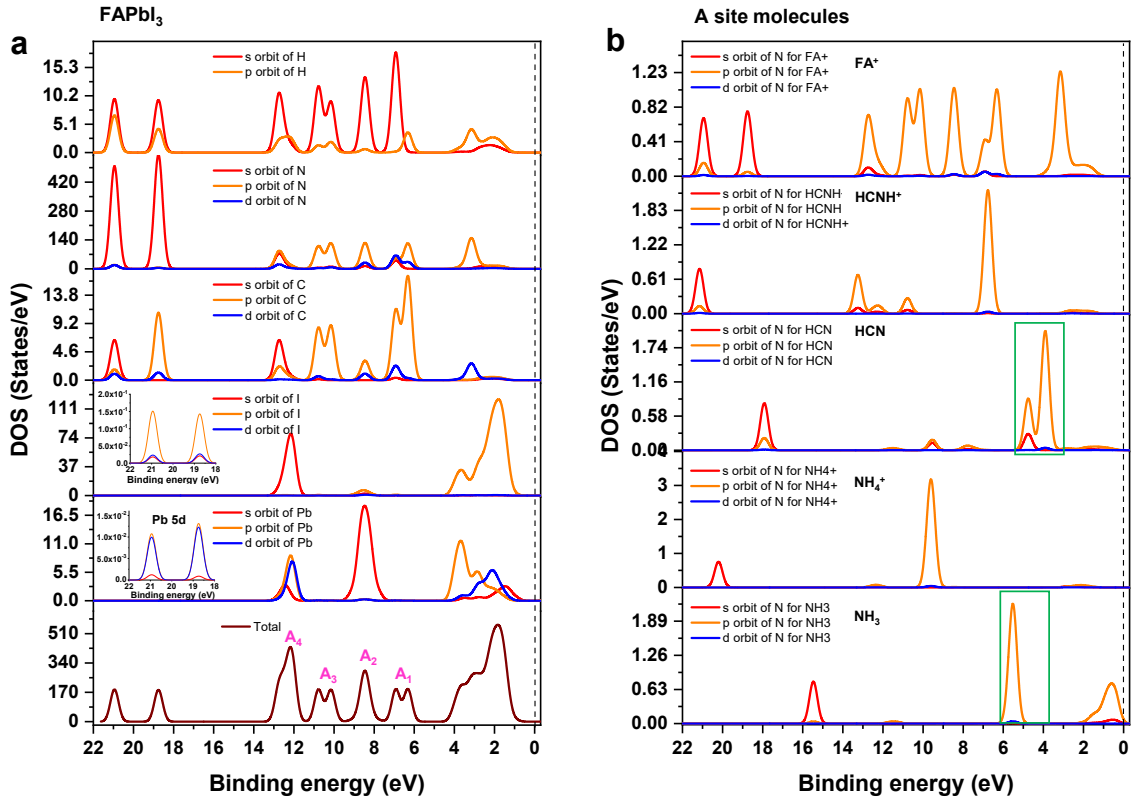

Figure S15. Computational analysis of the valence band. a, Total and orbital projected density of states (TDOS and PDOS) for pristine $FAPbI_3$ supercell as reference. **b,** Comparison of the partial density of states of N atoms in FA^+ of pristine and the above-mentioned substituted molecules. The first peak at 1.83 eV in VB indicates. On the other hand, it is seen that the energy Fermi levels of NH_3 and HCN-substituted $FAPbI_3$ are lowered compared to those in NH_4^+ and $HCNH^+$. The primary reason for this phenomenon is the introduction of the charge defect resulting in an overall positive charge of the periodic model system. PDOS for pristine $FAPbI_3$ and DMSs in Fig. S16 and S17 are aligned at the peaks of Pb 5d in the range of 16−22 eV according to the descriptions in the caption of Fig. S13. The green-coloured rectangular solid line in figure b may correspond to the marked "T" in Fig. S14.

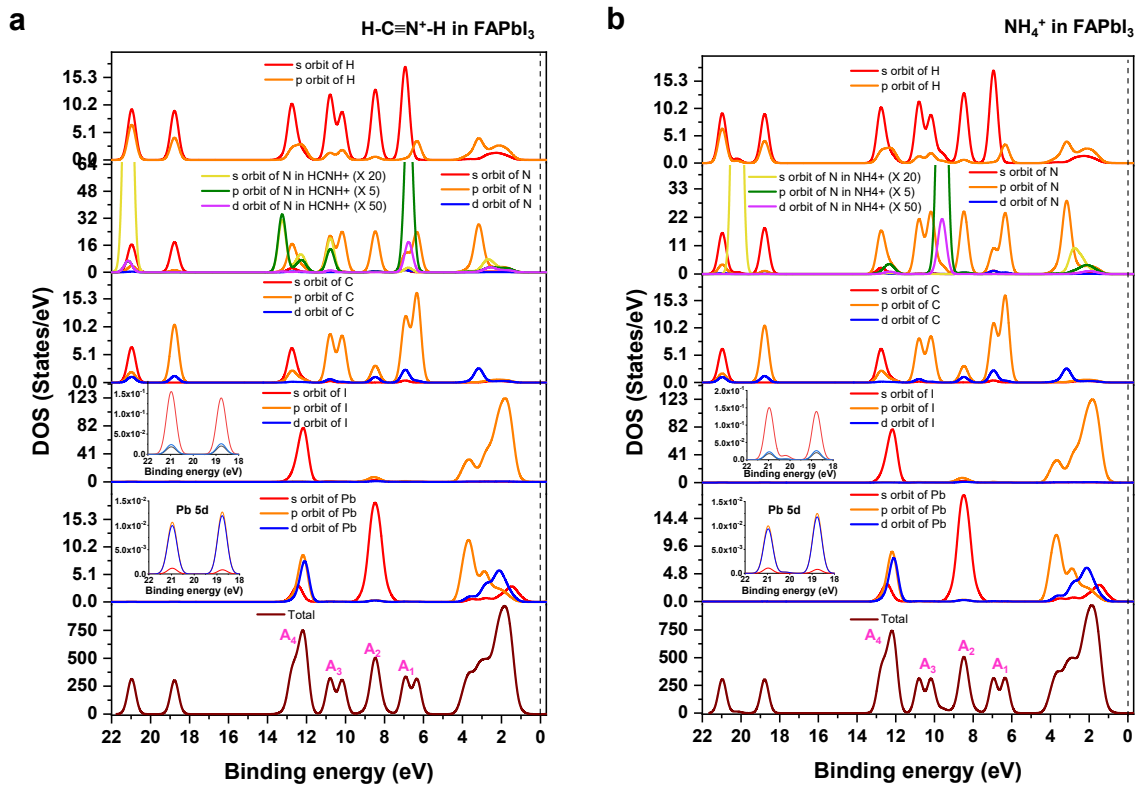

Figure S16. Computational analysis of the valence band. TDOS and PDOS for **a,** $HCNH^+$ and **b,** NH_4^+ substituted $FAPbI_3$ supercells, ranging from 22 eV to −0.3 eV. When PBP has substituted FA^+ at A site into $APbI_3$, first peak in VB (1.83 eV for pristine $FAPbI_3$ in Fig. S15(a)) are exhibited to red-shift (+) by 30 meV and 40 meV, when compared to the pristine $FAPbI_3$. There is a finite shift for NH_4^+ in the peak, almost identical to $FAPbI_3$. Therefore, these spectra have aligned with the spectra of pristine $FAPbI_3$ as displayed in Fig. 3(a). The reason for the shifting peaks is described in Content S1.

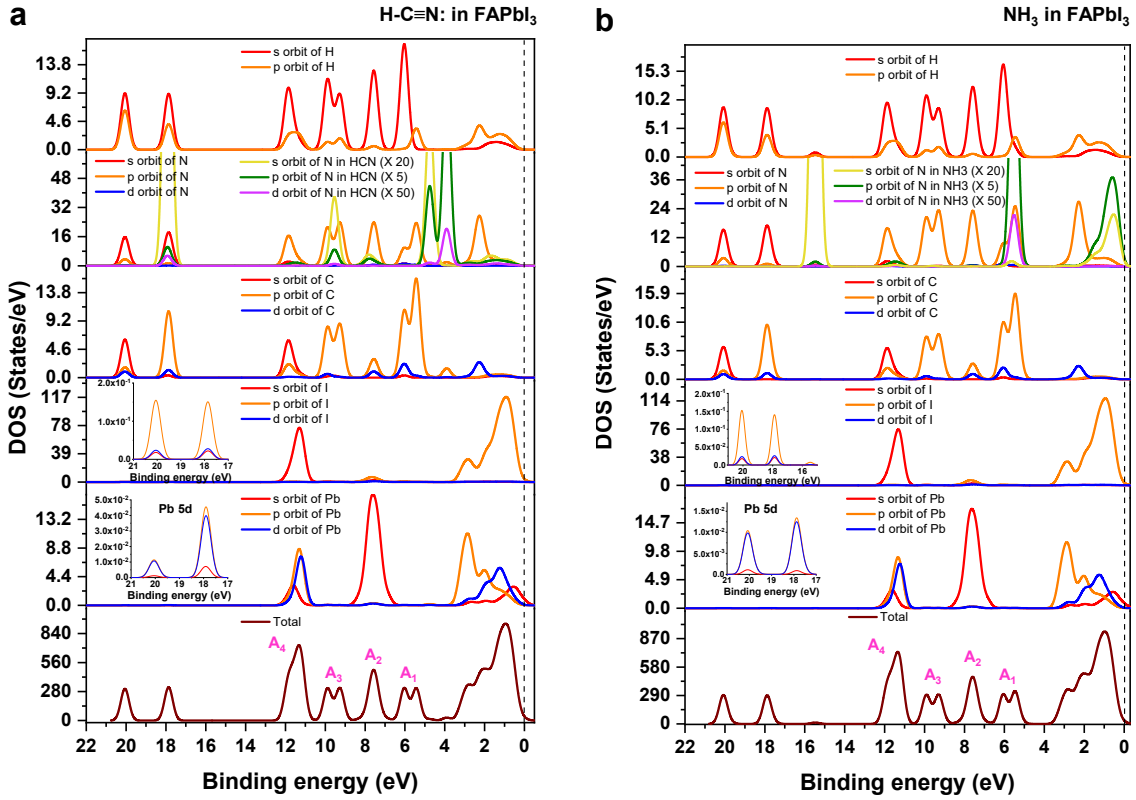

Figure S17. Computation analysis for valence band. TDOS and PDOS for **a,** HCN, and **b,** NH_3 substituted $FAPbI_3$ supercells in the range from 22 eV to −0.3 eV. We noticed that the blue-shifted peaks of −0.21 eV are affected by the introduction of DBP substituted a FA^+ into the position of the $FAPbI_3$ framework compared to that of the pristine $FAPbI_3$ (1.83 eV) in Fig. S15(a). Therefore, these spectra have aligned with the spectra of pristine $FAPbI_3$ as displayed in Fig. 3(a). The reason for shifting peaks is described in Content S1.

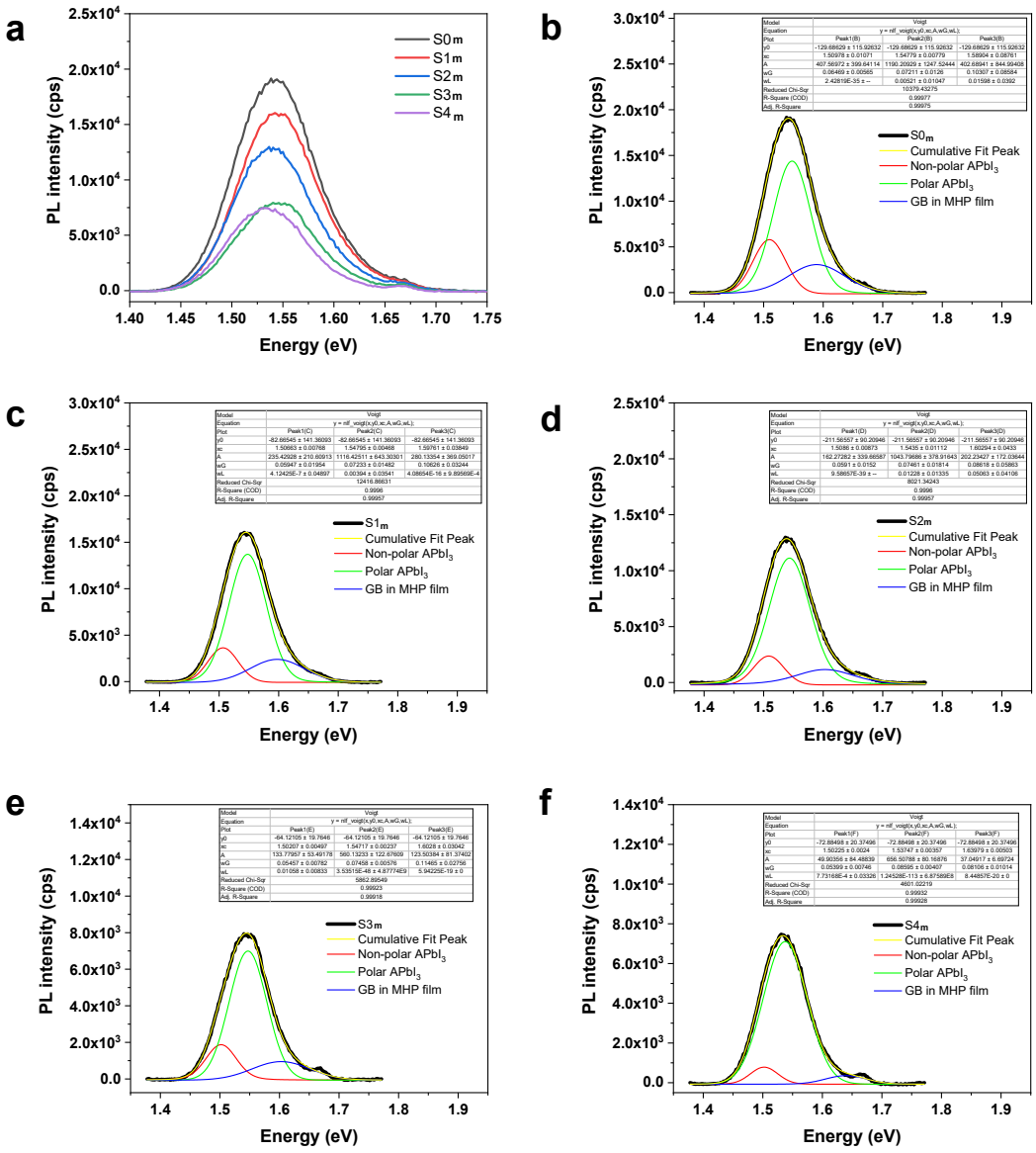

Figure S18. Steady state photoluminescence (PL) investigation. a, Scanned PL spectra from five post-annealing MHP_m films. The deconvoluted PL spectra have commonly defined to exist three PL components as Non-polar $APbI_3$(red coloured solid line), polar $APbI_3$ (green coloured solid line), and grain boundary (blue coloured solid line) in **b,** $S0_m$, **c,** $S1_m$, **d,** $S2_m$, **e,** $S3_m$ and **f,** $S4_m$ steps. The scanning PL spectra do not indicate symmetric Gaussian curve. Therefore, we perform to deconvolute PL spectra by Voigt function as reported in our previous work[Ref. S36]. We can finally make to identify three PL components as fitted curves in the blue, green, and red-coloured solid lines that are defined to GB, polar $FAPbI_3$, and non-polar $FAPbI_3$, respectively. The reason for defining the named three components can be explained in three previous works[Refs. S10, 37, 38]. The effect of polarizing GB component is possibly detected in the range of 1.6 eV −1.7 eV [Ref. S37] due to polarizing static lone pair[Ref. S38]. In the case of polaring $APbI_3$, a peak near 1.55 eV is detected due to an extended energy band gap through dynamic lone pair of octahedron[Ref.s S38]. PL spectra for non-polar $APbI_3$ as mostly formed α-$FAPbI_3$ detected a peak near 1.5 eV. The fitting results are summarized in Content Fig. S1(a).

Table S2. Steady-state photoluminescence investigation. The fitted parameters from deconvoluted PL spectra in Fig. S18 are summarized.

Post-annealing steps	Deconvoluted components	Integrated intensity (cps)	Fraction (%)	FWHM (eV)	Peak (eV)
$S0_m$	**Non-polar $APbI_3$**	235.429	14.426	0.059	1.507
	Polar $APbI_3$	1116.425	68.409	0.074	1.548
	GB in MHP	280.133	17.165	0.106	1.598
$S1_m$	**Non-polar $APbI_3$**	407.700	20.379	0.065	1.510
	Polar $APbI_3$	1190.209	59.493	0.075	1.548
	GB in MHP	402.689	20.128	0.112	1.589
$S2_m$	**Non-polar $APbI_3$**	162.273	11.523	0.059	1.510
	Polar $APbI_3$	1043.800	74.117	0.081	1.544
	GB in MHP	202.234	14.360	0.116	1.603
$S3_m$	**Non-polar $APbI_3$**	133.780	16.366	0.064	1.502
	Polar $APbI_3$	560.132	68.525	0.075	1.547
	GB in MHP	123.504	15.109	0.115	1.603
$S4_m$	**Non-polar $APbI_3$**	49.904	6.712	0.054	1.502
	Polar $APbI_3$	656.508	88.304	0.086	1.537
	GB in MHP	37.049	4.983	0.081	1.640

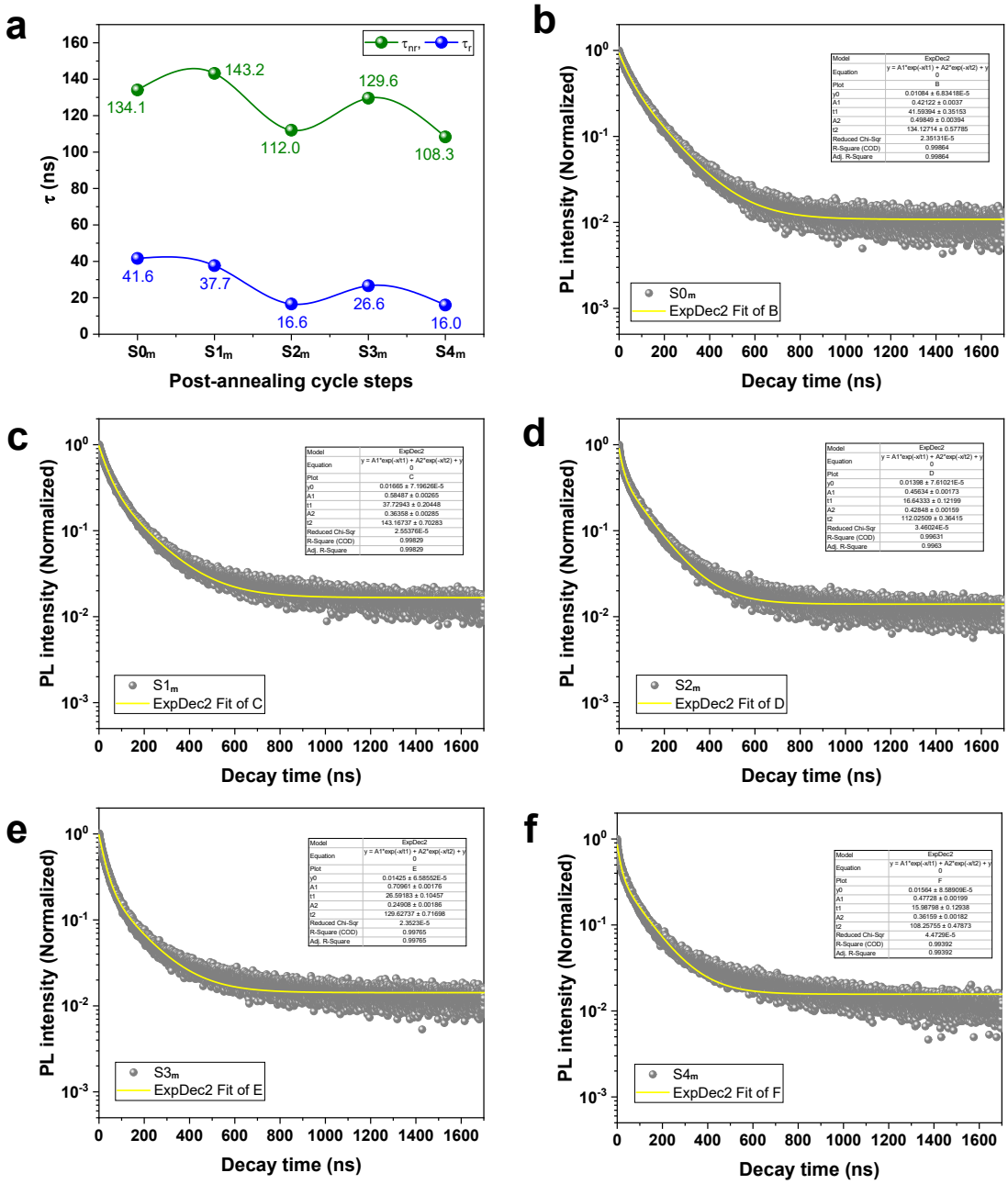

Figure S19. Time-resolved PL (TRPL) investigation. a, Summarized radiative (τ_r) and non-radiative (τ_{nr}) lifetimes are displayed from **b,** S0, **c,** S1, **d,** S2, **e,** S3 and **f,** S4 steps. τ_{eff} are obtained from an equation of $\tau_{eff} = (A_1\tau_1+A_2\tau_2)/(A_1+A_2)$ in previous report[Ref. S39] for estimated the relevant fraction of intragrain planar defect in MHP film. the result of τ_{eff} are summarized in Content Fig. S1(b). The value of A_n (n = 1, and 2) is the amplitude of counting photons at each components. **b-f,** Monitored TRPL spectra with bi-exponentially fitted parameters for five samples.

Table S3. Solar cell parameters from five PSCs. The defined solar cell parameters from five PSCs in Content Fig. S1(c) are summarized.

Steps (Samples)	PCE (%)	Fill factor (%)	V_{oc} (V)	J_{sc} (mA/cm^2)
$S0_m$	21.16	76.80	1.12	24.60
$S1_m$	22.46	79.80	1.12	25.13
$S2_m$	16.89	88.36	1.09	20.70
$S3_m$	14.05	73.50	1.08	17.70
$S4_m$	7.67	46.12	0.99	16.80

Supplemental References

1. A. Leonardi and P. Scardi, *Symposium: Neutron and X-Ray Studies of Advanced Materials VIII*, 2016, **47**, 5722–5732.
2. Z. Zhang, É. Ódor, D. Farkas, B. Jóni, G. Ribárik, G. Tichy, S.-H. Nandam, J. Ivanisenko, M. Preuss and T. Ungár, *Metall. Mater. Trans. A*, 2020, **51**, 513–530.
3. K. W. P. Orr, J. Diao, M. N. Lintangpradipto, D. J. Batey, A. N. Iqbal, S. Kahmann, K. Frohna, M. Dubajic, S. J. Zelewski, A. E. Dearle, T. A. Selby, Peng Li, T. A. S. Doherty, S. Hofmann, O. M. Bakr, I. K. Robinson and S. D. Stranks, *Adv. Mater.*, 2023, https://doi.org/10.1002/adma.202305549.
4. M. Jafari, M. Jamshidian, S. Ziaei-Rad, D. Raabe and F. Roters, *Int. J. Plast.*, 2017, **99**, 19-42.
5. A. García-Fernández, S. Svanström, C. M. Sterling, A. Gangan, A. Erbing, C. Kamal, T. Sloboda, B. Kammlander, G. J. Man, H. Rensmo, M. Odelius and U. B. Cappel, *Small*, 2022, **18**, 2106450.
6. B. Philippe, T. J. Jacobsson, J.-P. Correa-Baena, N. K. Jena, A. Banerjee, S. Chakraborty, U. B. Cappel, R. Ahuja, A. Hagfeldt, M. Odelius and H. Rensmo, *J. Phys. Chem. C*, 2017, **121**, 26655–26666.
7. A. Erbing, B. Philippe, B.-w. Park, U. B. Cappel, H. Rensmo and M. Odelius, *Chem. Sci.*, 2022, **13**, 9285-9294.
8. B.-w. Park, B. Philippe, S. M. Jain, X. Zhang, T. Edvinsson, H. Rensmo, B. Zietz and G. Boschloo, *J. Mater. Chem. A*, 2015, **3**, 21760-21771.
9. J.-S. Park, J. Calbo, Y.-K. Jung, L. D. Whalley and A. Walsh, *ACS Energy Lett.*, 2019, **4**, 1321–1327.
10. D. H. Fabini, G. Laurita, J. S. Bechtel, C. C. Stoumpos, H. A. Evans, A. G. Kontos, Y. S. Raptis, P. Falaras, A. V. d. Ven, M. G. Kanatzidis and R. Seshadri, *J. Am. Chem. Soc.*, 2016, **138**, 11820−11832.
11. M. Kroll, S. D. Öz, Z. Zhang, R. Ji, T. Schramm, T. Antrack, Y. Vaynzof, S. Olthof and K. Leo, *Sustainable Energy Fuels*, 2022, **6**, 3230-3239.
12. J. Zhou, Z. Liu, P. Yu, G. Tong, R. Chen, L. K. Ono, R. Chen, H. Wang, F. Ren, S. Liu, J. Wang, Z. Lan, Y. Qi and W. Chen, *Nat. Commun.* , 2023, **14**, 6120.
13. X. Zheng, C. Wu, S. K. Jha, Z. Li, K. Zhu and S. Priya, *ACS Energy Lett.* , 2016, **2**, 1014–1020.
14. M. Ghasemi, B. Guo, K. Darabi, T. Wang, K. Wang, C.-W. Huang, B. M. Lefler, L. Taussig, M. Chauhan, G. Baucom, T. Kim, E. D. Gomez, J. M. Atkin, S. Priya and A. Amassian, *Nat. Mater.*, 2023, **22**, 329–337.
15. B.-w. Park, J. Kim, T. J. Shin, Y. S. Kim, M. G. Kim and S. I. Seok, *Adv. Mater.*, 2023, **35**, 2211386.
16. W. T. M. V. Gompel, R. Herckens, G. Reekmans, B. Ruttens, J. D'Haen, P. Adriaensens, L. Lutsen and D. Vanderzande, *J. Phys. Chem. C.*, 2018, **122**, 4117–4124.
17. E. J. Juarez-Perez, L. K. Ono and Y. Qi, *J. Mater. Chem. A*, 2019, **7**, 16912-16919.
18. L. Ma, D. Guo, M. Li, C. Wang, Z. Zhou, X. Zhao, F. Zhang, Z. Ao and Z. Nie, *Chem. Mater.*, 2019, **31**, 8515–8522.
19. E. J. Juarez-Perez, L. K. Ono, M. Maeda, Y. Jiang, Z. Hawash and Q. Y., *J. Mater. Chem. A*, 2018, **6**, 9604-9612.
20. E. J. Juarez-Perez, Z. Hawash, S. R. Raga, L. K. Ono and Y. Qi, *Energy Environ. Sci.*, 2016, **9**, 3406-3410.
21. S. Tan, I. Yavuz, M. H. Weber, T. Huang, C.-H. Chen, R. Wang, H.-C. Wang, J. H. Ko, S. Nuryyeva, J. Xue, Y. Zhao, K.-H. Wei, J.-W. Lee and Y. Yang, *Joule*, 2020, **4**, 2426-

2442.
22. M. Yücel, B. M. Zabut, İ. Eroğlu and L. Türker, *J. Membr. Sci.* , 1995, **104**, 65-72.
23. R. S. Blake, P. S. Monks and A. M. Ellis, *Chem. Rev.* , 2009, **109**, 861–896.
24. Y.-T. Huang, S. R. Kavanagh, D. O. Scanlon, A. Walsh and R. L. Z. Hoye, *Nanotechnology*, 2021, **32**, 132004.
25. Y. Fu, S. Jin and X.-Y. Zhu, *Nat. Rev. Chem.*, 2021, **5**, 838-852.
26. J.-B. Li, Z.-K. Jiang, R. Wang, J.-Z. Zhao and R. Wang, *Npj Comput. Mater.*, 2023, **9**, Article number: 62.
27. J.-H. Lee, N. C. Bristowe, J. H. Lee, S.-H. Lee, P. D. Bristowe, A. K. Cheetham and H. M. Jang, *Chem. Mater.* , 2016, **28**, 4259−4266.
28. G. Divitini, S. Cacovich, F. Matteocci, L. Cinà, A. D. Carlo and C. Ducati, *Nat. energy*, 2016, **1**, Article number: 15012.
29. J. A. Steele, E. Solano, D. Hardy, D. Dayton, D. Ladd, K. White, P. Chen, J. Hou, H. Huang, R. A. Saha, L. Wang, F. Gao, J. Hofkens, M. B. J. Roeffaers, D. Chernyshov and M. F. Toney, *Adv. Energy Mater.*, 2023, **13**, 2300760.
30. A. Monshi, M. R. Foroughi and M. R. Monshi, *WJNSE*, 2012, **2**, 154-160.
31. R. Sivakami, S. Dhanuskodi and R. Karvembu, *Spectrochim. Acta A Mol. Biomol. Spectrosc.*, 2016, **152**, 43–50
32. G. K. Williamson and R. E. Smallman, *Philos. Mag.* , 2006, **1**, 34-46.
33. B. Kammlander, S. Svanström, D. Kühn, F. O. L. Johansson, S. Sinha, H. Rensmo, A. G. Fernández and U. B. Cappel, *Chem. Commun.*, 2022, **58**, 13523.
34. A. Majumdar, S. C. Das, T. Shripathi and R. Hippler, *Compos. Interfaces*, 2012, **19**.
35. A. V. Naumkin, A. Kraut-Vass, S. W. Gaarenstroom and C. J. Powell, *NIST Standard Reference Database 20, Version 4.1 (web version)*, 2012, http://dx.doi.org/10.18434/T18434T18488K.
36. B.-w. Park, H. W. Kwon, Y. Lee, D. Y. Lee, M. G. Kim, G. Kim, K.-j. Kim, Y. K. Kim, J. Im, T. J. Shin and S. I. Seok, *Nat. Energy*, 2021, **6**, 419–428.
37. A. A. Mamun, T. T. Ava, H. J. Jeong, M. S. Jeong and G. Namkoong, *Phys. Chem. Chem. Phys.*, 2017, **19**, 9143--9148.
38. K. M. McCall, V. Morad, B. M. Benin and M. V. Kovalenko, *ACS Materials Lett.*, 2020, **2**, 1218−1232.
39. W. Li, M. U. Rothmann, Y. Zhu, W. Chen, C. Yang, Y. Yuan, Y. Y. Choo, X. Wen, Y.-B. Cheng, U. Bach and J. Etheridge, *Nat. Energy*, 2021, **6**, 624–632.